nature genetics

Article

https://doi.org/10.1038/s41588-023-01337-7

Dual genetic tracing reveals a unique fibroblast subpopulation modulating cardiac fibrosis

Received: 1 May 2022

Accepted: 15 February 2023

Published online: 23 March 2023

Check for updates

Maoying Han[1,2,15], Zixin Liu[1,15], Lei Liu[2,15], Xiuzhen Huang[1], Haixiao Wang[1], Wenjuan Pu[1], Enci Wang[3], Xiuxiu Liu[1], Yan Li[1], Lingjuan He[4], Xufeng Li[5], Jiayu Wu[6], Lin Qiu[6], Ruling Shen[7], Qing-Dong Wang[8], Yong Ji[9], Reza Ardehali[10], Qiang Shu[11], Kathy O. Lui[12], Lixin Wang[3,13] & Bin Zhou[1,2,5,9,14]

After severe heart injury, fibroblasts are activated and proliferate excessively to form scarring, leading to decreased cardiac function and eventually heart failure. It is unknown, however, whether cardiac fibroblasts are heterogeneous with respect to their degree of activation, proliferation and function during cardiac fibrosis. Here, using dual recombinase-mediated genetic lineage tracing, we find that endocardium-derived fibroblasts preferentially proliferate and expand in response to pressure overload. Fibroblast-specific proliferation tracing revealed highly regional expansion of activated fibroblasts after injury, whose pattern mirrors that of endocardium-derived fibroblast distribution in the heart. Specific ablation of endocardium-derived fibroblasts alleviates cardiac fibrosis and reduces the decline of heart function after pressure overload injury. Mechanistically, Wnt signaling promotes activation and expansion of endocardium-derived fibroblasts during cardiac remodeling. Our study identifies endocardium-derived fibroblasts as a key fibroblast subpopulation accounting for severe cardiac fibrosis after pressure overload injury and as a potential therapeutic target against cardiac fibrosis.

Heart failure is a growing cause of mortality and morbidity worldwide[1]. Compared to other organs, the mammalian heart is among the least regenerative ones in adults, partly due to the poor proliferative capacity of cardiomyocytes[2,3]. In fact, cardiomyocytes only account for approximately 30% of the cells in the heart[4]; non-myocytes, including endothelial cells, fibroblasts and hematopoietic cells, are the most abundant cell types[5]. Of these, cardiac fibroblasts have a critical role in maintaining normal cardiac structures with mechanical and electrical functions, as well as regulating cardiac remodeling during pathological conditions, such as hypertension and myocardial infarction[6]. After heart injury, fibroblasts are activated and differentiate into contractile myofibroblasts that produce a large amount of extracellular matrix and generate collagen-rich scarring to replace dead cardiomyocytes[7,8]. Excessive accumulation of extracellular matrix profoundly impacts heart function by reducing wall compliance, eventually leading to heart failure[9]. In addition to these mechanical alterations, excessive scarring also promotes arrhythmia that can lead to sudden cardiac death and limits the regenerative potential of the injured myocardium during the progression of heart failure[10,11]. Given its important contribution to heart failure, understanding the pathophysiological processes and the underlying mechanisms driving cardiac fibrosis would help unravel new strategies for anti-fibrotic therapies[12,13].

Excessive cardiac myofibroblasts that emerge after injury are key mediators of tissue fibrosis and determinants of scar formation.

A full list of affiliations appears at the end of the paper. e-mail: zhoubin@sibs.ac.cn

The sources of cardiac myofibroblasts have been in dispute during the past decades. Notably, myofibroblasts are now believed to be derived from preexisting fibroblasts through proliferation[14]. Regarding the developmental origins of cardiac fibroblasts, two major distinct sources have been reported, including the epicardium and endocardium. Epicardial cells, the outermost layer of the mesothelial cells covering the developing heart, have the ability to migrate into the myocardium through epithelial–mesenchymal transition (EMT) and are differentiated into multiple cell lineages, such as fibroblasts, pericytes and smooth muscle cells[15–17]. Recent lineage tracing studies demonstrated that endocardial cells also contribute to fibroblasts, endothelial cells, pericytes and smooth muscle cells during cardiac development[18–21]. Despite these advances, it is unclear whether fibroblasts from different origins exhibit distinct functions during cardiac fibrosis. Understanding the in vivo role of unique fibroblast subpopulations accounting for tissue fibrosis would provide new insights into the identification of potential targets for treating cardiac fibrosis and preventing heart failure.

Results

Genetic tracing of endocardium-derived fibroblasts in the developing and adult heart

To specifically trace endocardium-derived fibroblasts, we used intersectional genetics that targeted endocardium-derived cells and fibroblasts using *Nfatc1-Dre*[22] and *Col1a2-CreER*[23], respectively (Fig. 1a). To enable readout of both Dre and Cre, we generated the *Rosa26-rox-Stop-rox-loxp-Stop-loxp-GFP* (*R26-RL-GFP*) mouse line (Extended Data Fig. 1a,b). When a *Tnnt2-Dre-Cre-tdTomato* mouse line (*Tnnt2-DCT*; Extended Data Fig. 1c) was crossed with *R26-RL-GFP*, green fluorescent protein (GFP) was activated in cardiomyocytes expressing tdTomato (Extended Data Fig. 1d–f). We also confirmed that one Stop alone could prevent GFP expression in *R26-RL-GFP* after crossing this mouse line with *CAG-Dre*[24] or *ACTB-Cre*[24] (Extended Data Fig. 1g–i). These data demonstrated that *R26-RL-GFP* was specific and efficient for dual lineage tracing in vivo. To specifically target endocardium-derived cells, we used the endocardium-specific *Nfatc1-Dre* driver for tracing[25,26]. Immunostaining on embryonic day 10.5 (E10.5) *Nfatc1-Dre;R26-RSR-tdTomato* embryonic sections showed that most tdTomato$^+$ cells did not express WT1 (Extended Data Fig. 2a–c). In addition, analysis of E17.5 *Nfatc1-Dre;R26-RSR-tdTomato* hearts revealed that *Nfatc1-Dre* mainly labeled endothelial cells and platelet-derived growth factor receptor-α (PDGFRα)$^+$ fibroblasts (Extended Data Fig. 2d–g). In the adult heart, we also observed a subset of PDGFRα$^+$ fibroblasts expressing GFP in the epicardial and subepicardial regions (Extended Data Fig. 2h,i), which could be due to unexpected activation of *Nfatc1-Dre* in fibroblasts after birth. In our study, *Col1a2-CreER*[23] was used to specifically label fibroblasts.

Having validated these mice, we generated *Nfatc1-Dre;Col1a2-CreER;R26-RL-GFP* mice to trace endocardium-derived fibroblasts (Fig. 1a). Dre-rox recombination removes the first Stop and subsequent Cre-*loxP* recombination removes the second Stop on tamoxifen (TAM) induction, leading to permanent genetic labeling of GFP in endocardium-derived fibroblasts (Fig. 1a). We found that GFP$^+$ endocardium-derived fibroblasts were derived from the endocardium after EMT transition in cushions and they were highly enriched in the ventricular septum (VS) and trabecular myocardium of the left ventricle (LV) in the developing heart (Extended Data Fig. 3 and Supplementary Note). Notably, endocardial cells in the trabecular layer minimally contributed to fibroblasts (Supplementary Fig. 1 and Supplementary Note). By injecting TAM into the endocardium-derived fibroblast tracer at different stages and collecting hearts for analysis at E17.5, we found that fibroblast cell fate was determined before E12.5, followed by subsequent fibroblast expansion at later developmental stages (Extended Data Fig. 4).

Furthermore, we examined the distribution of endocardium-derived fibroblasts in the adult heart by treating the endocardium-derived fibroblast tracer with TAM at 8–9 weeks of age (Fig. 1b). Immunostaining for PDGFRα and GFP on heart sections revealed highly enriched GFP$^+$ fibroblasts in the valves and a few GFP$^+$ cells in the upper part of the VS and inner part of the LV (Fig. 1c,d). Magnified images showed that a substantial portion of PDGFRα$^+$ cells expressed GFP in the valves and upper part of the VS (Fig. 1e,f), with relatively fewer GFP$^+$ endocardium-derived fibroblasts in the right ventricle (RV) and LV (Fig. 1g,h). Quantification of GFP$^+$ endocardium-derived fibroblasts in the myocardium showed that approximately 20% of PDGFRα$^+$ cells expressed GFP and virtually all GFP$^+$ cells expressed PDGFRα (Extended Data Fig. 5a–c). Flow cytometry analysis revealed that approximately 20% of PDGFRα$^+$ cells expressed GFP (Fig. 1i,j). We used additional markers such as vimentin to confirm fibroblast labeling and found that most GFP$^+$ cells were vimentin$^+$ but not α-smooth muscle actin (αSMA)$^+$ (Extended Data Fig. 5d–i). Because of the highly regional distribution pattern of GFP$^+$ endocardium-derived fibroblasts, especially in valves, we next quantified the percentage of GFP-expressing PDGFRα$^+$ fibroblasts in different regions of the myocardium. We found that GFP$^+$ endocardium-derived fibroblasts were highly enriched in the VS and the inner myocardial wall of the LV; they were substantially fewer in the outer myocardial wall of the LV and RV (Fig. 1k,l and Extended Data Fig. 2h,i). Thus, we established a dual genetic tracing system to specifically label endocardium-derived fibroblasts.

Endocardium-derived fibroblasts expand significantly after cardiac injury

We next asked whether endocardium-derived fibroblasts respond differently compared to epicardium-derived fibroblasts after cardiac injury. We crossed endocardium-derived fibroblast tracer with *R26-LSL-tdTomato*[27] to generate *Nfatc1-Dre;Col1a2-CreER;R26-RL-GFP;R26-LSL-tdTomato* knock-in mice, in which endocardium-derived fibroblasts would be labeled as GFP$^+$tdTomato$^+$ and fibroblasts from other origins (mainly epicardium-derived fibroblasts) would be marked as GFP$^-$tdTomato$^+$ (Fig. 2a). After 2 weeks of TAM washout, we performed transverse aortic constriction (TAC) to model pressure overload in mice and analyzed hearts at 4 days and 7 days after TAC (Fig. 2b). Immunostaining and flow cytometry, respectively, confirmed that GFP$^+$ and tdTomato$^+$ cells were fibroblasts but not endothelial cells in the sham or TAC hearts (Supplementary Fig. 2). While most cells expressing PDGFRα, vimentin or αSMA were still tdTomato$^+$, a substantial number of tdTomato$^+$ cells only weakly expressed these markers (Supplementary Fig. 3), which is consistent with previous studies showing reduced fibroblast marker expression after injury[28–31].

Based on the fact that myofibroblasts of the injured heart are derived from preexisting fibroblasts[18,32,33], we also used the lineage tracing reporter tdTomato, in addition to these fibroblast markers, to quantify fibroblasts and their derivatives in the injured heart. Whole-mount fluorescence imaging revealed pronounced GFP$^+$ signal enrichment in the VS of hearts at 4 days and 7 days after TAC, compared with sham treatment (Fig. 2c). Sirius Red staining showed severe tissue fibrosis in the upper part of the VS and upper and inner myocardial wall of the LV at 7 days after TAC (Fig. 2d). Immunostaining for tdTomato and GFP on heart sections revealed that GFP$^+$ fibroblasts were highly enriched in the upper part of the VS and inner myocardial wall of the LV at 4 days and 7 days after TAC, respectively (Fig. 2e,f), which is consistent with the regional pattern of tissue fibrosis evaluated using Sirius Red staining. We could barely detect any GFP$^+$ cells in the hearts of *Nfatc1-Dre;Col1a2-CreER;R26-RL-GFP* mice without TAM treatment at 28 d after TAC (Supplementary Fig. 4). Quantitation of flow cytometry analysis revealed that the percentage of PDGFRα$^+$ fibroblasts expressing GFP or the number of GFP$^+$ fibroblasts increased in the hearts at 4 days and 7 days after TAC, compared with that of sham controls (Fig. 2g and Supplementary Fig. 5), suggesting that endocardium-derived fibroblasts may have a higher proliferative potential than fibroblasts from other sources after TAC.

https://doi.org/10.1038/s41588-023-01337-7

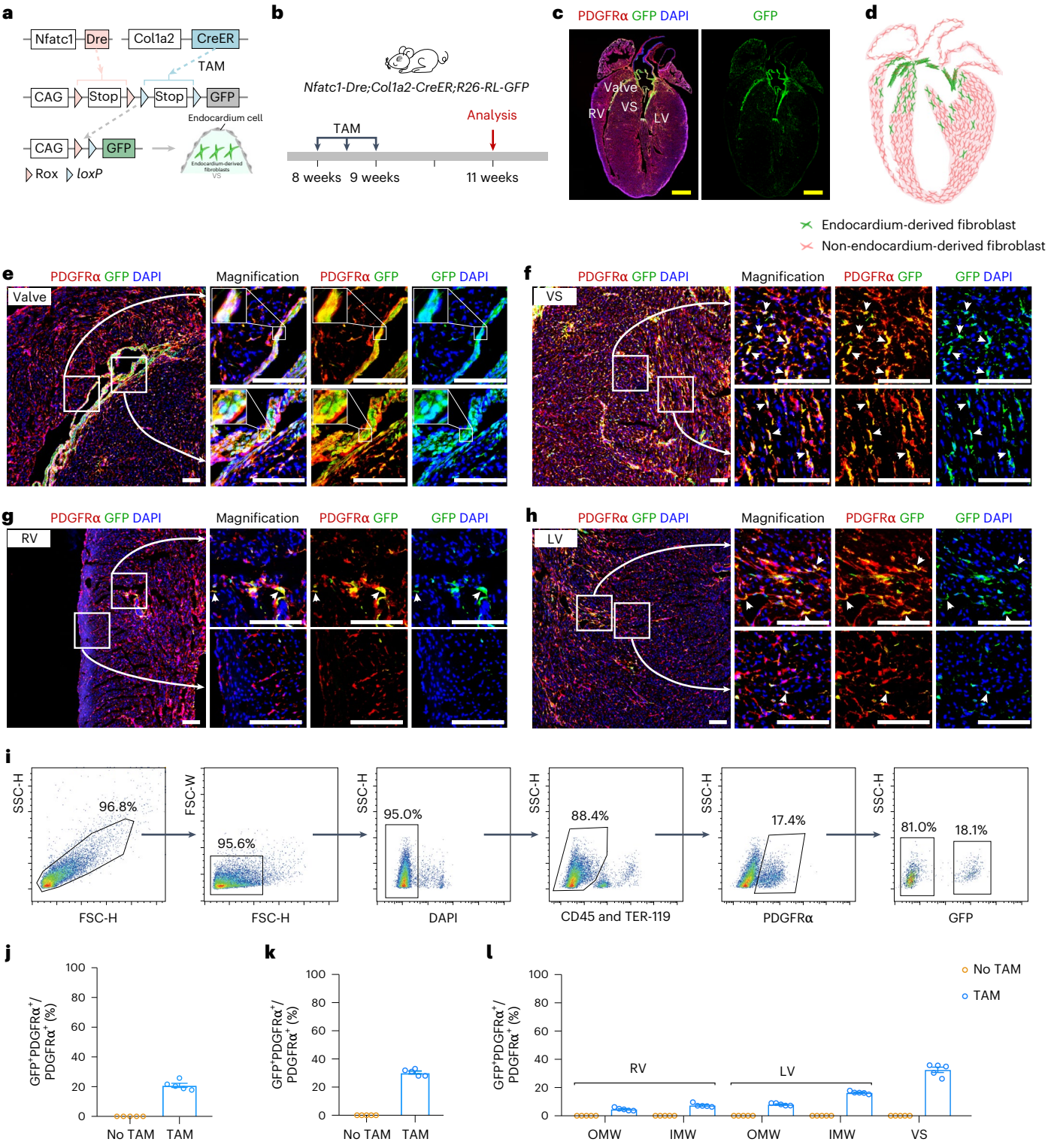

Fig. 1 | Distribution of endocardium-derived fibroblasts in the adult heart. **a**, Schematic showing the genetic tracing of endocardium-derived fibroblasts. **b**, Schematic showing the experimental strategy. **c**, Immunostaining for PDGFRα and GFP on whole adult heart sections. **d**, Cartoon image showing the distribution pattern of endocardium-derived fibroblasts in the adult heart. **e**–**h**, Immunostaining for PDGFRα and GFP on adult heart sections. The boxed regions are magnified in the panels on the right with split channels. The arrowheads indicate GFP$^+$PDGFRα$^+$ endocardium-derived fibroblasts. Images in e,f,g,h are regions of valve, VS, RV, LV, respectively. **i**, Flow cytometry analysis of the percentage of PDGFRα$^+$ endocardium-derived fibroblasts expressing GFP. **j**, Quantification of the percentage of PDGFRα$^+$ cells expressing GFP by FACS. **k**, Quantification of the percentage of PDGFRα$^+$ cells expressing GFP in heart valves and the myocardium. **l**, Quantification of the percentage of PDGFRα$^+$ endocardium-derived fibroblasts expressing GFP in different regions of the myocardium. OMW, outer myocardium wall; IMW, inner myocardium wall. All quantification data are represented as the mean ± s.e.m.; $n = 5$ mice. Scale bars, yellow, 1 mm; white, 100 μm. Each image is a representative of five individual mouse samples.

Given the significant expansion of endocardium-derived fibroblasts, we next analyzed the proliferation of GFP$^+$tdTomato$^+$ and GFP$^-$tdTomato$^+$ fibroblasts by a 5-ethynyl-2′-deoxyuridine (EdU) incorporation assay. A substantial number of GFP$^+$tdTomato$^+$ cells incorporated EdU in the upper part of the VS (VS^1) and upper myocardial wall of the LV (LV^1) at 4 days after TAC, while few GFP$^+$tdTomato$^+$ cells incorporated EdU in the lower part of the VS (VS^2) and lower part of the LV (LV^2) at 4 days after TAC (Fig. 2h). At 7 days after TAC, we found a few GFP$^+$tdTomato$^+$ cells incorporating EdU in the VS^1 and LV^1 regions but very few in the VS^2 and LV^2 regions (Fig. 2h). Notably, at 7 days after TAC, we detected many EdU$^+$ cells that were GFP$^-$tdTomato$^-$ (Fig. 2h), indicating proliferation of non-fibroblast lineages at 7 days after TAC. Quantification data revealed that the percentage of tdTomato$^+$ fibroblasts expressing GFP was highest in VS^1, medium in LV^1 and relatively lower in VS^2 and LV^2 of hearts at 4 days and 7 days after TAC (Fig. 2i). The percentage of tdTomato$^+$ fibroblasts incorporating EdU was significantly higher in GFP$^+$ than GFP$^-$ population in the VS^1 of hearts at 4 days and 7 days after TAC (Fig. 2j). Independently, we used PDGFRα, vimentin and αSMA and found a significantly higher proliferation rate in GFP$^+$ endocardium-derived fibroblasts compared with GFP$^-$ fibroblasts after TAC (Supplementary Figs. 6 and 7). At 28 days after TAC, we found that these GFP$^+$ endocardium-derived fibroblasts still remained regional in the heart and expressed PDGFRα and vimentin but no longer maintained αSMA expression (Extended Data Fig. 6).

Contribution of epicardium-derived fibroblasts to cardiac fibrosis after TAC

We next labeled epicardium-derived fibroblasts and determined if they proliferated and expanded in regions of severe fibrosis, such as the upper region of the VS. To lineage-trace epicardium-derived fibroblasts, we crossed the epicardium-specific Cre driver *Wt1-CreER*[17] with *R26-LSL-tdTomato*[27] (Fig. 3a). We induced epicardial labeling at the embryonic stage when EMT occurs and performed TAC at the adult stage (8 weeks old) followed by analysis at 4 days and 7 days after TAC (Fig. 3b). We found that tdTomato$^+$ cells were widely distributed in the hearts but noticeably fewer tdTomato$^+$ cells were observed in the VS^1 and inner layer of the LV, such as papillary muscle (Fig. 3c), complementary to the endocardium-derived fibroblast distribution pattern in the heart at homeostasis or after TAC (Figs. 1c,d and 2e,f). Quantification revealed few PDGFRα$^+$ fibroblasts being tdTomato$^+$ in VS^1, while most PDGFRα$^+$ fibroblasts were tdTomato$^+$ in VS^2 (Fig. 3d,e). These data demonstrated that epicardium-derived fibroblasts minimally expanded into regions where endocardium-derived fibroblasts were mainly distributed in the adult heart after TAC.

To investigate the extent of proliferation in epicardium-derived fibroblasts at 4 days and 7 days after TAC, we performed EdU incorporation assays and assessed EdU$^+$ epicardium-derived fibroblasts in different parts of the heart. We did not detect noticeable EdU incorporation in tdTomato$^+$PDGFRα$^+$ cells of sham-treated hearts (Supplementary Fig. 8a–c). We found few tdTomato$^+$PDGFRα$^+$ epicardium-derived fibroblasts incorporating EdU at 4 days or 7 days after TAC in the VS^1 (Fig. 3f). In contrast, tdTomato$^+$PDGFRα$^+$ epicardium-derived fibroblasts incorporating EdU could be readily detected in the LV^1 at 4 days and 7 days after TAC (Fig. 3f). Quantification data showed that 1.67% ± 0.068%, 2.32% ± 0.396%, 6.26% ± 0.601% and 1.977% ± 0.101% of tdTomato$^+$PDGFRα$^+$ epicardium-derived fibroblasts incorporated EdU, respectively, in VS^1, VS^2, LV^1 and LV^2 at 4 days after TAC, while 1.46% ± 0.072%, 1.72% ± 0.148%, 3.98% ± 0.487% and 1.33% ± 0.175% of tdTomato$^+$PDGFRα$^+$ epicardium-derived fibroblasts incorporated EdU, respectively, in VS^1, VS^2, LV^1 and LV^2 at 7 days after TAC (Fig. 3g), suggesting that epicardium-derived fibroblasts proliferated mainly in the LV^1. Moderate proliferation of epicardium-derived fibroblasts was still noticed in some regions of the LV^1 and left atrium after TAC (Fig. 3h and Supplementary Fig. 8d–f).

Highly regional proliferation of fibroblasts after TAC

We next took advantage of a genetic approach to trace cell proliferation, that is, ProTracer[34], to assess fibroblast proliferation after TAC. We generated a fibroblast-specific proliferation tracing system, Fb-ProTracer. In this design, we generated *Col1a2-CreER;Ki67-LSL-2A-Dre;R26-RL-GFP* mice in which TAM-induced *Col1a2-CreER* would remove Stop in *Ki67-LSL-2A-Dre*, yielding a new *Ki67-2A-Dre* allele, and remove the first Stop in the *R26-RL-GFP* allele (Fig. 4a). Initial TAM treatment primed *Ki67-2A-Dre* to start continuous recording of cell proliferation only in fibroblasts over time (Fig. 4a). In the sham-treated heart, we found sporadic GFP$^+$ cells three weeks after TAM treatment (Fig. 4b,c). Immunostaining for PDGFRα and GFP on heart sections revealed that all GFP$^+$ cells expressed PDGFRα (Fig. 4d), confirming fibroblast-specific recording of proliferation.

We next exposed the Fb-ProTracer mice to TAC and analyzed the injured hearts at 4 days and 7 days after TAC (Fig. 4e). Whole-mount fluorescence imaging highlighted increased GFP$^+$ signals in the TAC samples compared with that of sham-treated group (Fig. 4f). Sirius Red staining of Fb-ProTracer hearts showed regional severe fibrosis at 4 days and 7 days after TAC (Fig. 4g). Immunostaining for PDGFRα and GFP on heart sections showed highly enriched GFP$^+$ fibroblasts in the upper part of the VS and some regions of the LV (Fig. 4h), confirming the severe regional fibrosis pattern revealed by Sirius Red staining (Fig. 4g). Quantification data revealed a significantly increased percentage of PDGFRα$^+$ fibroblasts expressing GFP after TAC compared with that of sham-treated mice (Fig. 4i). Notably, the most pronounced increase in fibroblast proliferation was apparent in the VS^1, followed by the LV^1 and then the other regions (Fig. 4i). Taken together, proliferation tracing based on Fb-ProTracer revealed highly regional fibroblast generation after TAC (Fig. 4j), the pattern of which mostly recapitulated the expansion of endocardium-derived fibroblasts in severely fibrotic regions (Fig. 2e,f).

Fig. 2 | Endocardium-derived fibroblasts expand regionally during cardiac fibrosis after TAC. a, Schematic showing simultaneous tracing of general and endocardium-derived fibroblasts. **b**, Schematic showing the experimental design. **c**, Whole-mount fluorescence views of hearts collected from *Nfatc1-Dre;Col1a2-CreER;R26-RL-GFP;R26-LSL-tdTomato* mice under sham treatment or at 4 days or 7 days after TAC. The inserts show brightfield images. **d**, Sirius Red staining of heart sections. **e**, Immunostaining for tdTomato and GFP on whole heart sections from mice at 4 days or 7 days after TAC. **f**, Cartoon images showing the distribution of endocardium-derived fibroblasts in hearts. **g**, Flow cytometry analysis of the percentage of endocardium-derived fibroblasts expressing GFP in the hearts of sham- or TAC-treated mice. **h**, Immunostaining for tdTomato, GFP and EdU on different heart sections collected from mice at 4 days or 7 days after TAC. The arrowheads point to EdU$^+$ endocardium-derived fibroblasts. **i**, Quantification of the percentage of endocardium-derived fibroblasts expressing GFP in different parts of the heart. Data are the mean ± s.e.m.; $n = 5$ mice. **j**, Quantification of the percentage of GFP$^+$tdTomato$^+$ fibroblasts (endocardium-derived fibroblasts) or GFP$^-$tdTomato$^+$ fibroblasts (non-endocardium-derived fibroblasts) incorporating EdU in the hearts collected from mice at 4 days or 7 days after TAC. Data are the mean ± s.e.m.; 4 d after TAC graph, $n = 6$ mice; VS^1: endocardium-derived fibroblasts versus non-endocardium-derived fibroblasts, $^*P < 0.0001$; LV^1: endocardium-derived fibroblasts versus non-endocardium-derived fibroblasts, $^*P = 0.0425$; 7 days after TAC graph, $n = 5$ mice; VS^1: endocardium-derived fibroblasts versus non-endocardium-derived fibroblasts, $^*P < 0.0001$; NS, not significant. Statistical analysis was performed using two-way analysis of variance (ANOVA) with Šidák's multiple comparisons test. Scale bars, yellow, 1 mm; white, 100 μm. Each image is representative of five individual mouse samples.

https://doi.org/10.1038/s41588-023-01337-7

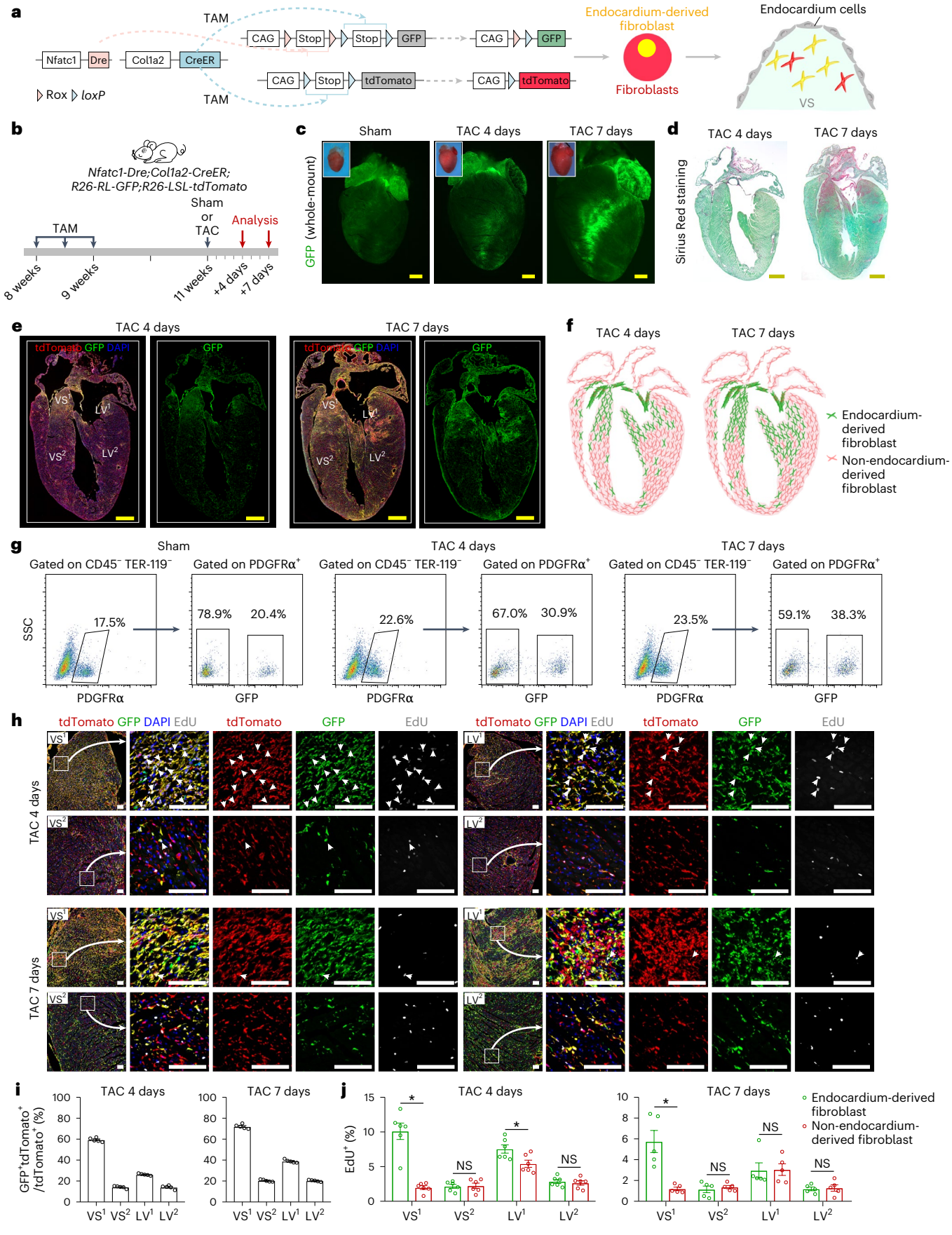

https://doi.org/10.1038/s41588-023-01337-7

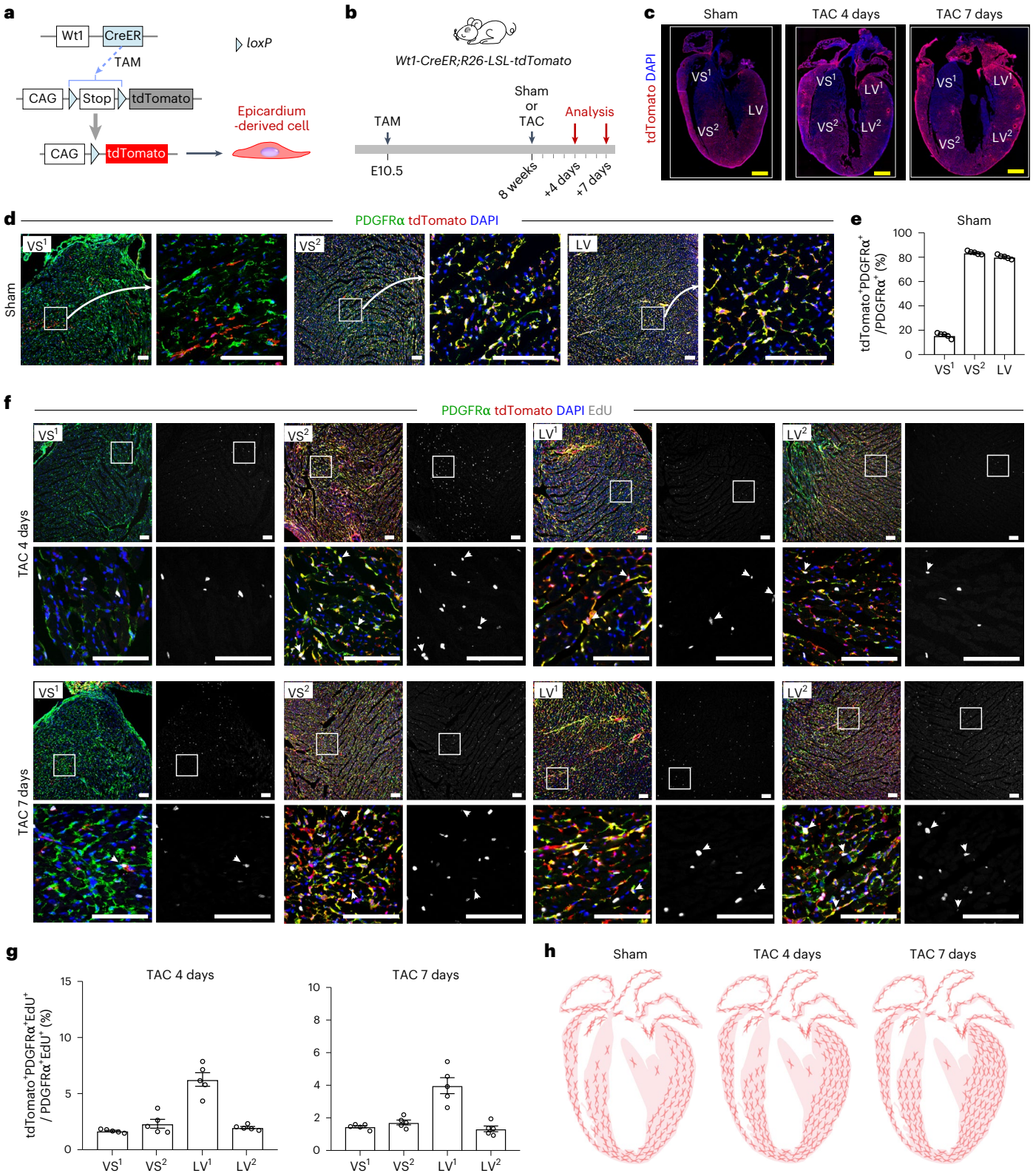

Fig. 3 | Contribution of epicardium-derived fibroblasts to cardiac fibrosis after TAC. a, Schematic showing the lineage-tracing strategy of embryonic epicardium-derived cells. **b**, Schematic showing the experimental design. **c**, Immunostaining for tdTomato and DAPI on whole heart sections from *Wt1-CreER;R26-LSL-tdTomato* mice 4 days or 7 days after TAC compared with the hearts of sham-treated mice. **d**, Immunostaining for PDGFRα and tdTomato on hearts of sham-treated mice. **e**, Quantification of PDGFRα$^+$ fibroblasts expressing tdTomato on the VS and LV zones of the heart sections. **f**, Immunostaining for PDGFRα, tdTomato and EdU on different parts of the heart collected from mice at 4 days or 7 days after TAC. The arrowheads indicate tdTomato$^+$PDGFRα$^+$EdU$^+$ fibroblasts. **g**, Quantification of tdTomato$^+$PDGFRα$^+$ fibroblasts incorporating EdU in different parts of the heart sections collected from mice 4 days or 7 days after TAC. **h**, Cartoon images showing the distribution of epicardium-derived fibroblasts in the hearts of sham- or TAC-treated mice. All quantification data are presented as the mean ± s.e.m.; $n = 5$ mice. Scale bars, yellow, 1 mm; white, 100 μm. Each image is representative of five individual mouse samples.

https://doi.org/10.1038/s41588-023-01337-7

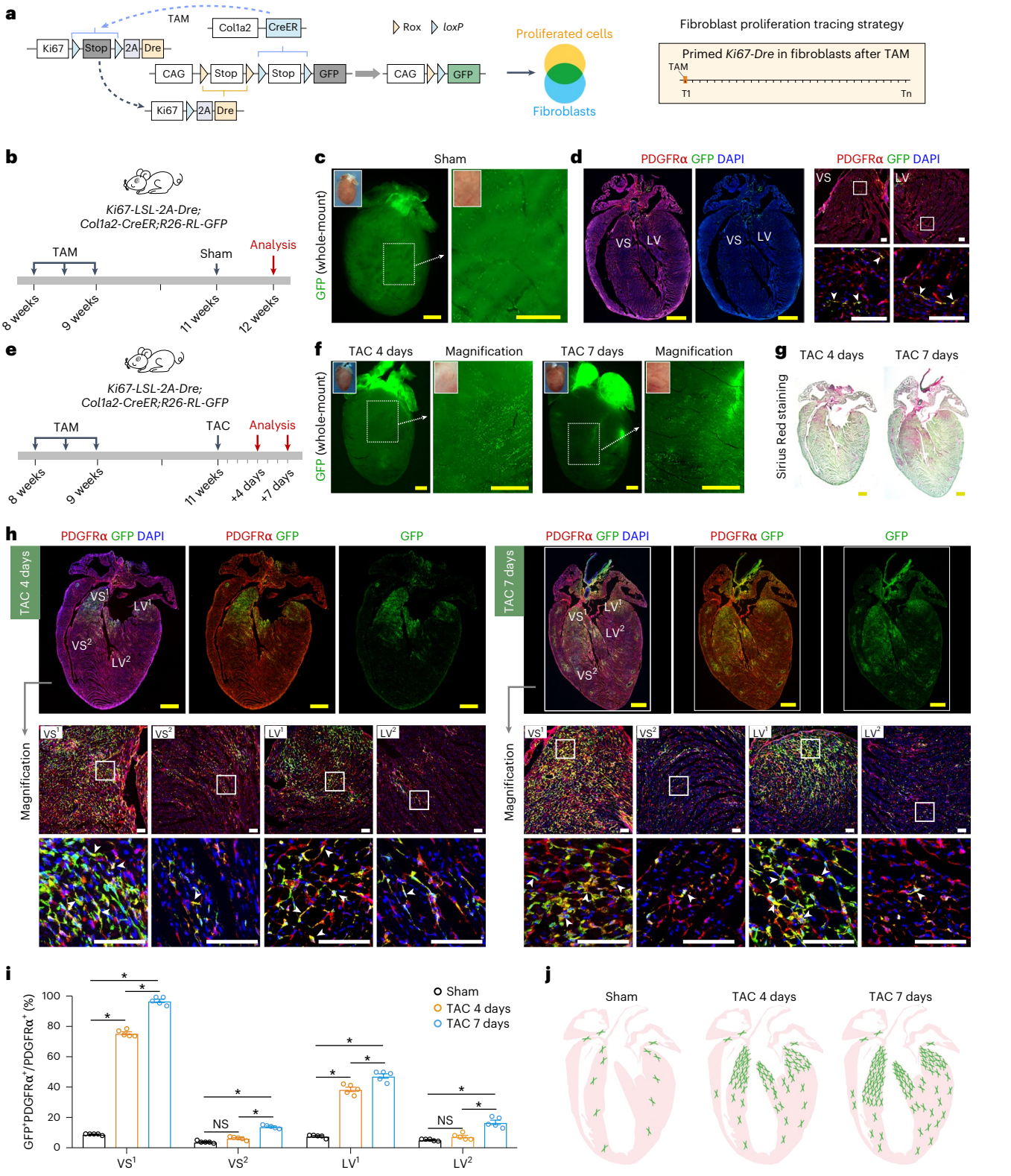

Fig. 4 | Fibroblast-specific proliferation tracing reveals regional fibroblast proliferation after TAC. a, Schematic showing the fibroblast-specific proliferation tracing strategy. *Col1a2-CreER* induced the *Ki67-LSL-2A-Dre* allele, which primes the system to continuously record Ki67$^+$ fibroblasts from time point 1 (T1) to time point n (Tn). **b**, Schematic showing the experimental design. **c**, Whole-mount and epifluorescence images of hearts collected from mice 3 weeks after TAM injection. **d**, Immunostaining for PDGFRα and GFP on heart sections. The arrowheads indicate PDGFRα$^+$GFP$^+$ fibroblasts. **e**, Schematic showing the experimental design. **f**, Whole-mount and epifluorescence images of hearts collected from mice 4 days or 7 days after TAC. **g**, Sirius Red staining of TAC heart sections. **h**, Immunostaining for PDGFRα and GFP on heart sections collected from mice at 4 days or 7 days after TAC. The arrowheads indicate PDGFRα$^+$GFP$^+$ fibroblasts. **i**, Quantification of the percentage of PDGFRα$^+$ fibroblasts expressing GFP in different parts of the hearts from sham- or TAC-treated mice. Data are the mean ± s.e.m. $n = 5$ mice; in each comparison group, $^*P < 0.0001$. Statistical analysis was performed using two-way ANOVA with Tukey's multiple comparisons test. **j**, Cartoon images showing regional distribution of proliferated fibroblasts in hearts after TAC. Scale bars, yellow, 1 mm; white, 100 μm. Each image is representative of five individual mouse samples.

Genetic ablation of endocardium-derived fibroblasts alleviates cardiac fibrosis

To determine the role of endocardium-derived fibroblasts in cardiac fibrosis after pressure overload injury, we generated *Nfatc1-Dre;Col1a2-CreER;R26-LSL-RSR-tdT-DTR* mice (endocardium-derived fibroblast-diphtheria toxin receptor (DTR)), in which Dre-rox and Cre-*loxP* recombinations mediate simultaneous expression of tdTomato and DTR specifically in endocardium-derived fibroblasts (Fig. 5a). We treated endocardium-derived fibroblast-DTR mice with diphtheria toxin (DT) and confirmed that tdTomato$^+$ fibroblasts were significantly reduced in the hearts after DT treatment compared to PBS-treated ones (Extended Data Fig. 7a–g). Under normal conditions, there was no significant difference in heart function of DT- and PBS-treated hearts (Extended Data Fig. 7h,i). We next induced TAC injury two weeks after TAM, injected DT or PBS one week after TAC and collected hearts for analysis four weeks after TAC (Fig. 5b). We found strong tdTomato$^+$ signals in the hearts of endocardium-derived fibroblast-DTR mice treated with PBS but sparse tdTomato$^+$ signals in those treated with DT (Fig. 5c). Sirius Red staining highlighted severe fibrosis in mice treated with PBS, most of which were enriched in the VS^1 and LV^1 (Fig. 5d). In contrast, fibrosis was remarkably reduced in the hearts of DT-treated mice (Fig. 5d,e), indicating that genetic ablation of endocardium-derived fibroblasts alleviated the severity of cardiac fibrosis after TAC.

We next performed immunostaining to examine the distribution of endocardium-derived fibroblasts in the hearts of PBS- and DT-treated endocardium-derived fibroblast-DTR mice. We found that tdTomato$^+$ endocardium-derived fibroblasts were highly enriched in the VS^1 and LV^1 of PBS-treated hearts, whereas very few tdTomato$^+$ endocardium-derived fibroblasts remained in the DT-treated ones (Fig. 5f). Quantitatively, there was a significant reduction in the percentage of PDGFRα$^+$ fibroblasts expressing tdTomato in the hearts of DT-treated mice than in the PBS-treated group (Fig. 5g). Echocardiography demonstrated severely depressed ejection fraction (EF) and fractional shortening (FS), measures of systolic contractile function, in mice treated with PBS after TAC (Fig. 5h,i). In contrast, significantly less functional deterioration as evidenced by EF and FS was observed in DT-treated mice than in the PBS-treated group after TAC (Fig. 5h,i), indicating that endocardium-derived fibroblast ablation reduced function decline after injury. Additionally, hematoxylin and eosin (H&E) staining of heart sections revealed significantly reduced cross-sectional area in DT-treated hearts than in the PBS-treated group after TAC (Fig. 5j,k). The heart-to-body weight ratio was increased in the PBS-treated group after TAC but was significantly attenuated in DT-treated mice (Fig. 5l). Likewise, cardiomyocyte size measured by wheat germ agglutinin (WGA) was increased after TAC but was significantly attenuated after DT treatment (Fig. 5m,n).

Wnt signaling promotes endocardium-derived fibroblast expansion after TAC

To explore the potential molecular mechanisms, we isolated GFP$^+$ and GFP$^-$ fibroblasts from the ventricular myocardium of *Nfatc1-Dre;Col1a2-CreER;R26-RL-GFP* mice for gene expression analysis (Fig. 6a and Extended Data Fig. 8a). Principal component analysis (PCA) revealed that GFP$^+$ fibroblasts of sham-treated mice were more similar to the activated GFP$^+$ fibroblasts of TAC than GFP$^-$ fibroblasts of sham-treated mice (Fig. 6b). In both sham-treated and TAC hearts, GFP$^+$ fibroblasts showed profound changes in their transcriptional profile with many differentially expressed genes (DEGs) relative to that of GFP$^-$ fibroblasts (Fig. 6c). Genes associated with fibroblast activation[28,35,36], such as *Thbs4*, *Cilp*, *Postn*, *Comp*, *Fmod*, *Cthrc1* and *Ddah1* were upregulated in GFP$^+$ fibroblasts compared with GFP$^-$ ones (Fig. 6c). Gene set enrichment analysis (GSEA) showed positive regulation of canonical Wnt signaling pathway and fibroblast proliferation in GFP$^+$ compared to GFP$^-$ fibroblasts of both sham-treated and TAC groups (Fig. 6d). In particular, Wnt pathway genes, such as *Wnt10b*, *Ccn4*, *Wnt9a*, *Fzd4*, *Fzd7*, *Sox9*, *Lzts2* and *Dkk3* were upregulated in GFP$^+$ fibroblasts compared with GFP$^-$ ones of both sham-treated and TAC groups, as demonstrated by the heatmap in Fig. 6e. In addition to genes of the cell cycle and Wnt signaling pathways, other pathways related to wound healing, ossification and extracellular matrix organization were also upregulated in GFP$^+$ fibroblasts compared to GFP$^-$ ones (Extended Data Fig. 8b). These data suggest that genes related to fibroblast activation and proliferation are more significantly upregulated in GFP$^+$ than GFP$^-$ fibroblasts after TAC.

To understand the impact of anatomical locations on gene expression, we isolated GFP$^+$ and GFP$^-$ fibroblasts from the upper and lower parts of the ventricle at 7 days after TAC (Fig. 6f). PCA revealed that GFP$^+$ fibroblasts of the upper and lower parts were clustered next to each other, while GFP$^-$ fibroblasts of the upper and lower parts were also clustered closely in TAC hearts (Fig. 6g). To dissect the impact of developmental origins on gene expression, we analyzed differential gene expression in GFP$^+$ and GFP$^-$ fibroblasts of the upper regions and found that many fibroblast activation genes, such as *Cilp*, *Thbs4*, *Postn*, *Fmod* and *Ddah1* were upregulated in GFP$^+$ fibroblasts compared with GFP$^-$ ones (Fig. 6h). To evaluate the impact of anatomical locations on gene expression after injury, we analyzed differential gene expression in GFP$^+$ fibroblasts of the upper and lower regions of the heart and found that genes related to angiogenesis, such as *Pecam1*, *Hey1*, *Cdh5* and *Kdr* were significantly upregulated in the upper region of the heart (Fig. 6i). Moreover, Gene Ontology (GO) enrichment analysis revealed that the developmental origins mainly affected expression of genes associated with wound healing, ossification, extracellular matrix, Wnt signaling, cell adhesion and migration, endocardial cushion and hypertrophy

Fig. 5 | Genetic ablation of endocardium-derived fibroblasts alleviates cardiac fibrosis and reduces the decline of heart function after TAC. **a**, Schematic showing specific endocardium-derived fibroblast ablation by dual recombinase-mediated genetic approach using *Nfatc1-Dre;Col1a2-CreER;R26-LSL-RSR-tdT-DTR* mice. **b**, Schematic showing the experimental design. **c**, Whole-mount brightfield and fluorescence views of hearts collected from mice after PBS or DT injection 28 days after TAC. **d**, Sirius Red staining of heart sections from PBS- or DT-treated TAC mice. **e**, Quantification of fibrotic areas in different areas of TAC hearts after PBS or DT treatment. Data are the mean ± s.e.m. $n = 5$ mice; VS^1: PBS versus DT, $^*P < 0.0001$; LV^1: PBS versus DT, $^*P < 0.0001$. **f**, Immunostaining for PDGFRα and tdTomato on heart sections collected from PBS- or DT-treated mice. The arrowheads indicate PDGFRα$^+$tdTomato$^+$ endocardium-derived fibroblasts. **g**, Quantification of PDGFRα$^+$ fibroblasts expressing tdTomato in different areas of hearts after PBS or DT treatment. Data are the mean ± s.e.m. $n = 5$ mice; VS^1: PBS versus DT, $^*P < 0.0001$; VS^2: PBS versus DT, $^*P = 0.0001$; LV^1: PBS versus DT, $^*P < 0.0001$; LV^2: PBS versus DT, $^*P < 0.0001$. **h**,**i**, Quantification of EF and FS of mice treated with PBS or DT at different time points after TAC. In **h**, data are the mean ± s.e.m. $n = 5$ mice; TAC 14 days, PBS versus DT, $^*P = 0.0147$; TAC 28 days, PBS versus DT, $^*P < 0.0001$. In **i**, data are the mean ± s.e.m. $n = 5$ mice; TAC 28 days, PBS versus DT, $^*P = 0.0016$. **j**, H&E staining of sham-treated or TAC heart sections collected from mice treated with PBS or DT. **k**, Quantification of the relative cross-sectional area of hearts. Data are the mean ± s.e.m. $n = 5$ mice; sham-wild type (WT) versus TAC-PBS, $^*P = 0.0001$; TAC-PBS versus TAC-DT, $^*P = 0.0217$. **l**, Quantification of heart-to-body weight ratio in mice after Sham or TAC. **m**, Immunostaining for WGA on sham or TAC hearts. Data are the mean ± s.e.m.; $n = 5$ mice; sham-WT versus TAC-PBS and TAC-PBS versus TAC-DT, $^*P < 0.0001$. **n**, Quantification of the cardiomyocyte cross-sectional area of hearts. Data are the mean ± s.e.m. $n = 5$ mice; sham-WT versus TAC-PBS and TAC-PBS versus TAC-DT, $^*P < 0.0001$. Scale bars, yellow, 1 mm; white, 100 μm; magenta, 50 μm. Each image is representative of five individual mouse samples. In **e** and **g**–**i**, statistical analysis was performed by two-way ANOVA with Šidák's multiple comparisons test; in **k**, **l** and **n**, one-way ANOVA with Tukey's multiple comparisons test was used.

https://doi.org/10.1038/s41588-023-01337-7

adaptation, which were upregulated in GFP⁺ fibroblasts compared with GFP⁻ ones (Fig. 6j). In contrast, distinct anatomical regions mainly influenced expression of genes associated with interleukin production and angiogenesis (Fig. 6j). We also found that differential gene expression of GFP⁺ versus GFP⁻ fibroblasts among all fibroblasts of the entire ventricle mainly reflected the impact on

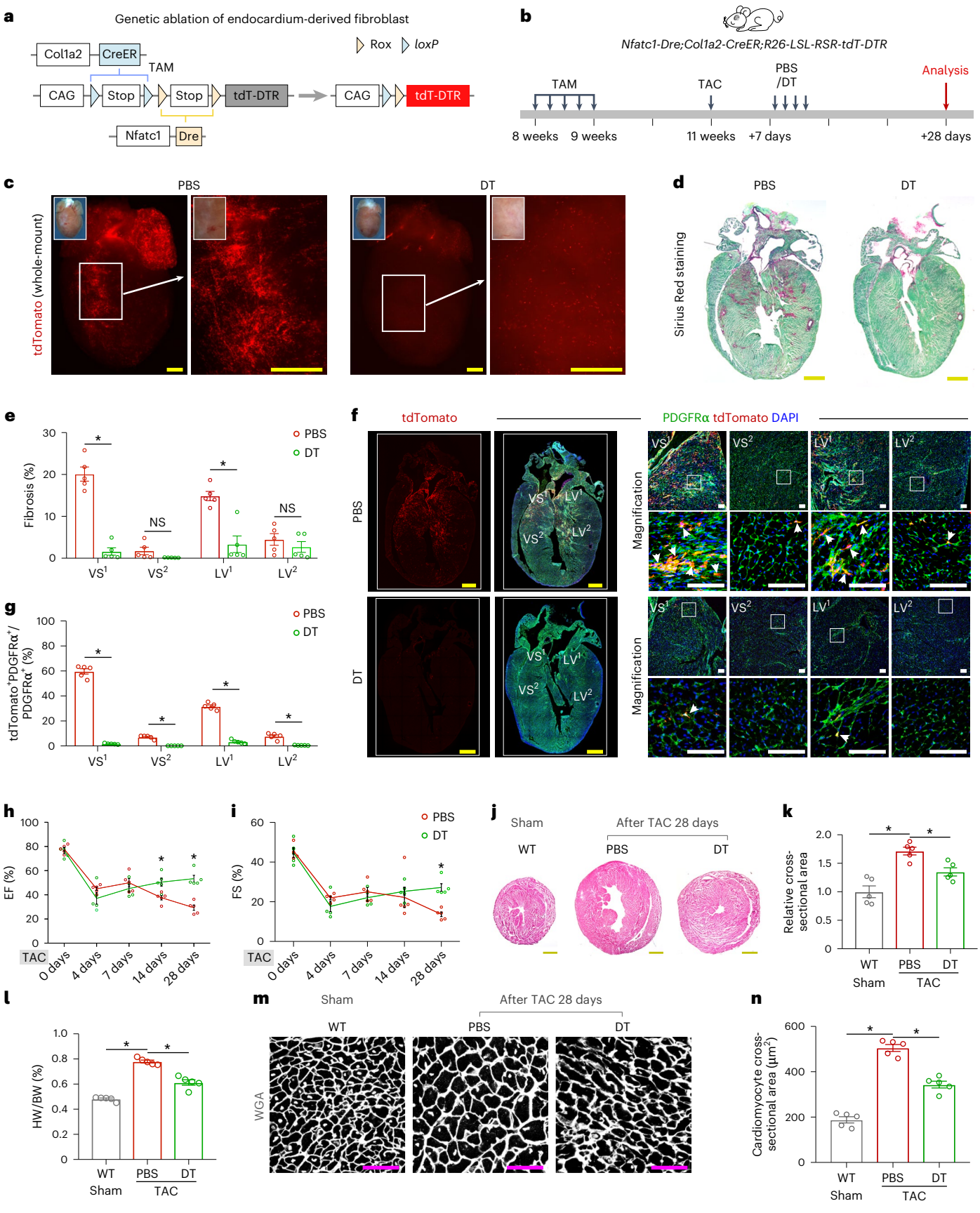

https://doi.org/10.1038/s41588-023-01337-7

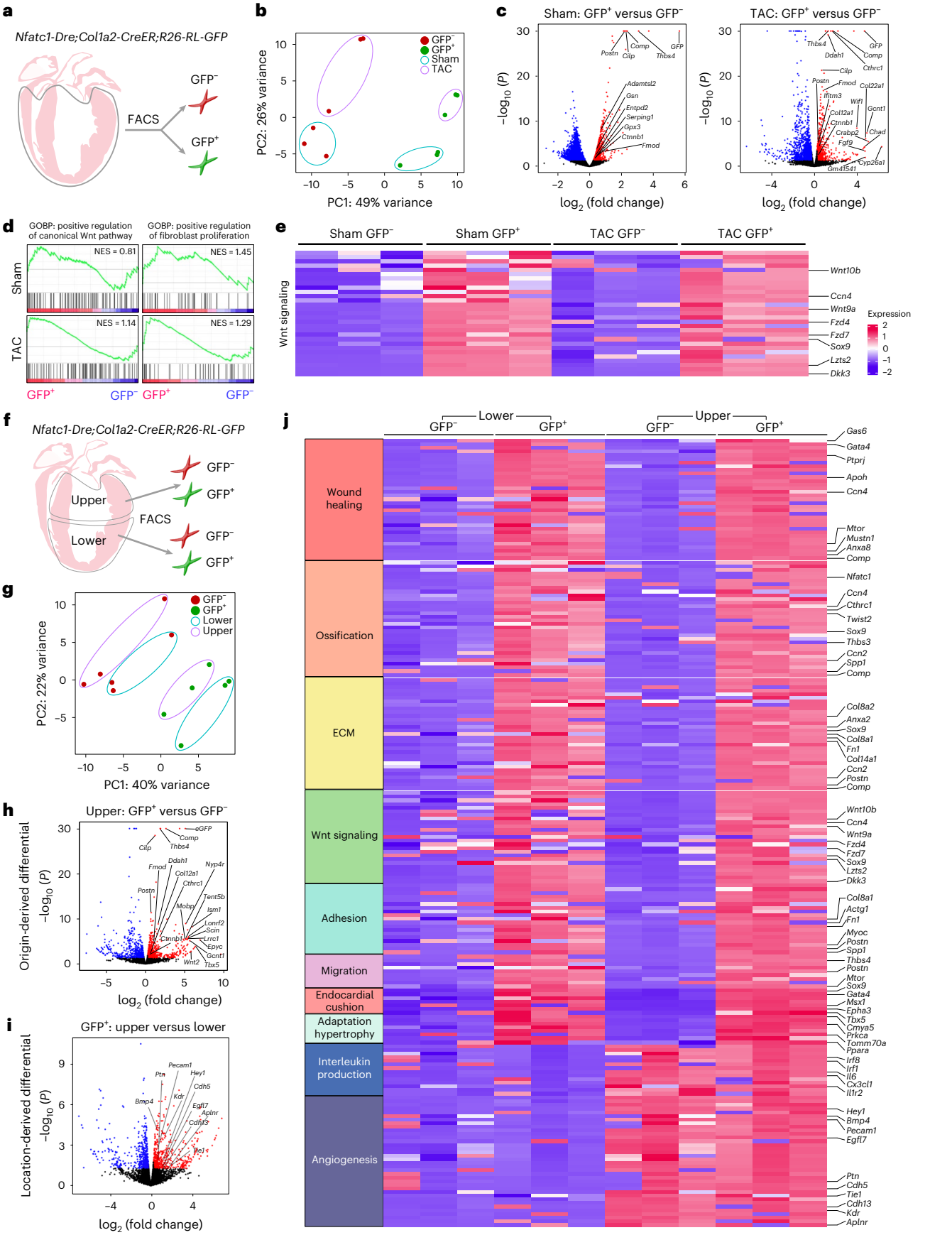

the developmental origins because they shared more DEGs with those determined by developmental origins than anatomical regions (Extended Data Fig. 8b–d).

With reference to the upregulated genes of the Wnt signaling pathway in endocardium-derived fibroblasts, we next investigated whether Wnt signaling functionally regulates the expansion of

Fig. 6 | Gene profiles of endocardium- and epicardium-derived fibroblasts in adult hearts after TAC. a, Schematic diagram showing the experimental design. **b**, PCA of GFP$^+$ and GFP$^-$ fibroblasts isolated from the hearts of sham-treated or TAC group. **c**, Volcano plots showing DEGs in GFP$^+$ fibroblasts versus GFP$^-$ fibroblasts from the sham-treated or TAC group. **d**, GSEA of positive regulation of canonical Wnt signaling pathway or positive regulation of fibroblast proliferation in GFP$^+$ and GFP$^-$ fibroblasts from the sham-treated or TAC group. GOBP, GO biological process; NES, normalized enrichment score. **e**, Gene expression heatmap of the scaled expression of Wnt signaling pathway-related genes in GFP$^-$ and GFP$^+$ fibroblasts from the sham-treated or TAC group. **f**, Schematic diagram showing the experimental design. **g**, PCA of GFP$^+$ and GFP$^-$ fibroblasts isolated from the upper and lower parts of the heart. **h**,**i**, Volcano plots showing differential gene expression in GFP$^+$ versus GFP$^-$ fibroblasts from the upper (**h**) or lower (**i**) part of the heart. **j**, Gene expression heatmap of the scaled expression of selected GO pathway-related genes in GFP$^-$ and GFP$^+$ fibroblasts from the lower or upper part of the heart. $n = 3$ mice; in **c**, **h** and **i**, statistical analysis was performed by Wald test. ECM, extracellular matrix.

endocardium-derived fibroblasts during cardiac fibrosis by specifically deleting *Ctnnb1* in endocardium-derived fibroblasts. To achieve this goal, we developed a dual recombinase-mediated sequential genetic approach by first generating *Nfatc1-Dre;Col1a2-RSR-CreER;Ctnnb1-flox* mice (Fig. 7a). In this design, *Nfatc1-Dre* removes rox-Stop-rox within *Col1a2-RSR-CreER* after Dre-rox recombination, yielding a *Col1a2-CreER* allele (Fig. 7a). Regarding *Col1a2-RSR-CreER*, both Dre and TAM were required to activate CreER for recombination (Supplementary Fig. 9). Like the endocardium-derived fibroblast tracer, we confirmed that *Nfatc1-Dre;Col1a2-RSR-CreER;R26-RL-GFP* specifically and efficiently targeted endocardium-derived fibroblasts in the adult heart (Extended Data Fig. 9). To simultaneously trace endocardium-derived fibroblasts and delete *Ctnnb1* in endocardium-derived fibroblasts, we generated *Nfatc1-Dre;Col1a2-RSR-CreER;R26-RL-GFP;Ctnnb1-fl* as mutant mice and their littermate *Nfatc1-Dre;Col1a2-RSR-CreER;R26-RL-GFP;Ctnnb1-wt* as controls, for analysis after TAC (Fig. 7b). TAM-induced Cre-*loxP* recombination removed the *loxP*-flanked *Ctnnb1* exons, resulting in functional gene ablation specifically in endocardium-derived fibroblasts (Fig. 7a,b). Quantitative PCR with reverse transcription (RT–qPCR) targeting *Ctnnb1* showed significantly reduced gene expression levels in isolated GFP$^+$ fibroblasts of mutant mice compared with controls (Fig. 7c). We also found significantly reduced levels of *Ctnnb1* in GFP$^+$ compared to GFP$^-$ fibroblasts, indicating the specificity of gene deletion in endocardium-derived fibroblasts (Extended Data Fig. 10a,b). Endocardium-derived fibroblast-specific deletion of *Ctnnb1* resulted in reduced β-catenin protein expression in GFP$^+$ fibroblasts, which did not impair heart function under normal conditions (Extended Data Fig. 10c–e).

We found strong GFP$^+$ signals in controls mice that were much weaker in the hearts of mutant mice (Fig. 7d) and a significant reduction in the number of GFP$^+$ endocardium-derived fibroblasts in the VS and some parts of the LV (Fig. 7e,f). Sirius Red staining showed less severe fibrosis in the hearts of mutant than control mice after TAC (Fig. 7g,h), indicating that *Ctnnb1* depletion in endocardium-derived fibroblasts limited the progression of cardiac fibrosis. Echocardiography demonstrated significantly decreased EF and FS in control mice, which were significantly greater in mutant than in control mice (Fig. 7i,j), indicating that *Ctnnb1* deletion in endocardium-derived fibroblasts reduced the decline of heart function after TAC. H&E staining of heart sections revealed significantly reduced cardiac hypertrophy in the hearts of mutant than control mice after TAC (Fig. 7k,l). The ratio of heart weight to body weight after TAC was also increased in the hearts of control compared to sham-treated mice, whereas the ratio was significantly attenuated in the hearts of mutant compared to control mice (Fig. 7m). Cardiomyocyte size measured by WGA staining revealed that cardiomyocyte hypertrophy was inhibited in the hearts of mutant compared with control mice after TAC (Fig. 7n,o). The reduced endocardium-derived fibroblast number and abrogated fibrosis in *Ctnnb1* knockout mice was mainly due to reduced cell proliferation but not increased apoptosis after TAC (Supplementary Figs. 10 and 11 and Supplementary Note). We did not observe valve defects in mutant mice (Supplementary Fig. 12 and Supplementary Note). These data demonstrated that deletion of *Ctnnb1* in endocardium-derived fibroblasts significantly reduced cardiac fibrosis and preserved cardiac function after pressure overload injury.

Discussion

Identifying a specific fibroblast subpopulation endowed with fibrogenic potential in vivo is a critical step toward effectively manipulating their responses after injury to limit tissue fibrosis in many diseases[37]. In this study, we developed dual recombinase-mediated genetic systems to specifically trace endocardium-derived fibroblasts after pressure overload injury (Fig. 8). Our lineage-tracing data suggested that endocardium-derived fibroblasts proliferated more significantly than epicardium-derived fibroblasts in regions prone to develop severe fibrosis after TAC. Genetic ablation of endocardium-derived fibroblasts demonstrated that they were responsible for the development of severe cardiac fibrosis after TAC and also reduction in heart function. Mechanistically, inhibiting Wnt signaling in endocardium-derived fibroblasts significantly reduced their expansion, inhibited the progression of cardiac fibrosis and reduced the decline of heart function after TAC (Fig. 8). Our study uncovered previously unappreciated

Fig. 7 | *Ctnnb1* knockout reduces cardiac fibrosis and the decline of heart function after TAC. a, Schematic diagram showing sequential intersectional genetic strategy for dual recombinase-mediated *Ctnnb1* gene ablation in endocardium-derived fibroblasts. R1 and R2 indicate the Dre-rox and Cre-*loxP* recombinations, respectively. **b**, Schematic diagram showing the experimental design. **c**, RT–qPCR of *Ctnnb1* expression in GFP$^+$ fibroblasts isolated from control and mutant mice. Data are the mean ± s.e.m. $n = 5$ mice; $^*P < 0.0001$. **d**, Whole-mount fluorescence images of hearts from control and mutant mice. **e**, Immunostaining for PDGFRα and GFP on heart sections from control and mutant mice. **f**, Quantification of PDGFRα$^+$ fibroblasts expressing GFP in different heart areas 28 days after TAC. Data are the mean ± s.e.m. $n = 5$ mice; VS^1: control versus mutant, $^*P < 0.0001$; VS^2: control versus mutant, $^*P = 0.0298$; LV^1: control versus mutant, $^*P < 0.0001$; **g**, Sirius Red staining of heart sections from control and mutant mice. **h**, Quantification of fibrotic areas in different heart areas 28 days after TAC. Data are the mean ± s.e.m. $n = 5$ mice; VS^1: control versus mutant; LV^1: control versus mutant, $^*P < 0.0001$. **i**,**j**, Quantification of EF and FS of control and mutant mice at different time points after TAC. In **i**, data are the mean ± s.e.m. $n = 5$ mice; TAC 28 days, control versus mutant, $^*P = 0.0049$. In **j**, data are the mean ± s.e.m. $n = 5$ mice; TAC 28 days, control versus mutant, $^*P = 0.0223$. **k**, H&E staining of heart sections collected from control or mutant mice. **l**, Quantification of the relative cross-sectional area of hearts. Data are the mean ± s.e.m. $n = 5$ mice; sham-WT versus TAC-control, $^*P < 0.0001$; TAC-control versus TAC-mutant, $^*P = 0.0163$. **m**, Quantification of the heart-to-body weight ratio of control or mutant mice. Data are the mean ± s.e.m. $n = 5$ mice; sham-WT versus TAC-control, $^*P < 0.0001$; TAC-control versus TAC-mutant, $^*P = 0.0004$. **n**, Immunostaining for WGA of heart sections. **o**, Quantification of the cardiomyocyte cross-sectional area of hearts collected from control or mutant mice. Data are the mean ± s.e.m. $n = 5$ mice; sham-WT versus TAC-control and TAC-control versus TAC-mutant, $^*P < 0.0001$. In **c**, statistical analysis was performed using an unpaired Student's *t*-test. In **f** and **h**–**j**, statistical analysis was performed using a two-way ANOVA with Šidák's multiple comparisons test. In **l**, **m** and **o**, statistical analysis was performed using a one-way ANOVA with Tukey's multiple comparisons test. Scale bars, yellow, 1 mm; white, 100 μm; magenta, 50 μm. Each image is representative of five individual biological samples.

https://doi.org/10.1038/s41588-023-01337-7

functions of a unique fibroblast subpopulation derived from the endocardium in regulating cardiac fibrosis after TAC. Targeting unique fibroblasts using new technologies such as CAR T cells[38,39] could be considered for treating cardiac fibrosis (Supplementary Note). Our work also highlighted the importance of using dual recombinase-mediated genetic systems to study specific functions of a particular cell subset within heterogeneous cell populations during disease progression (Supplementary Note).

In this study, we mainly focused on pressure overload-induced cardiac fibrosis. It is probable that different subpopulations of fibroblasts may respond to different injury models in a cell-specific manner. For example, epicardial cells were activated to respond to

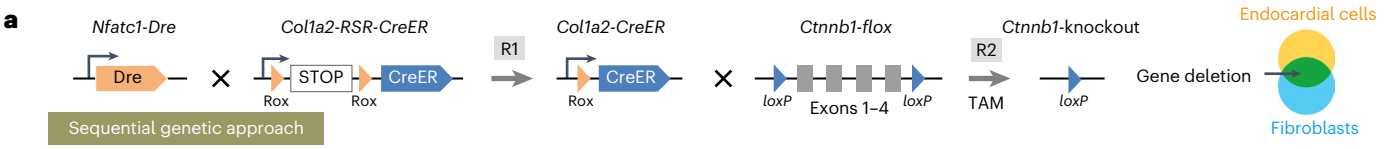

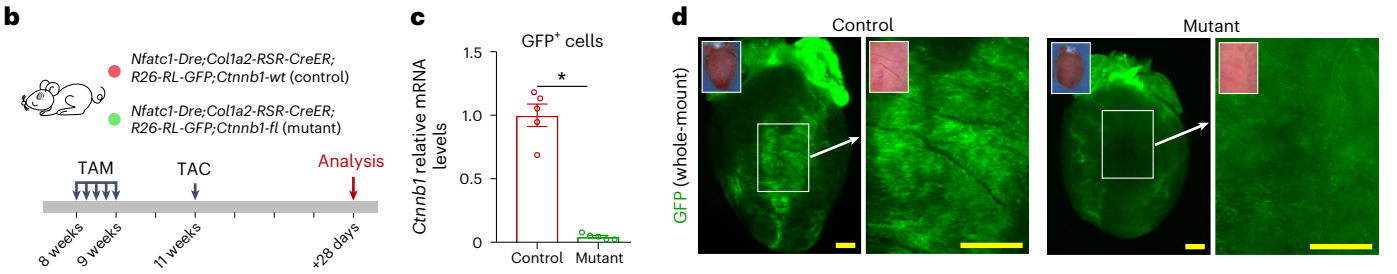

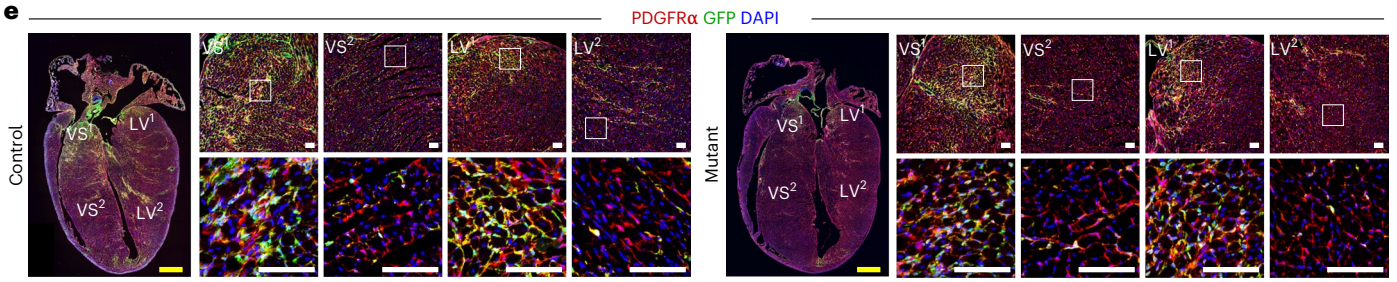

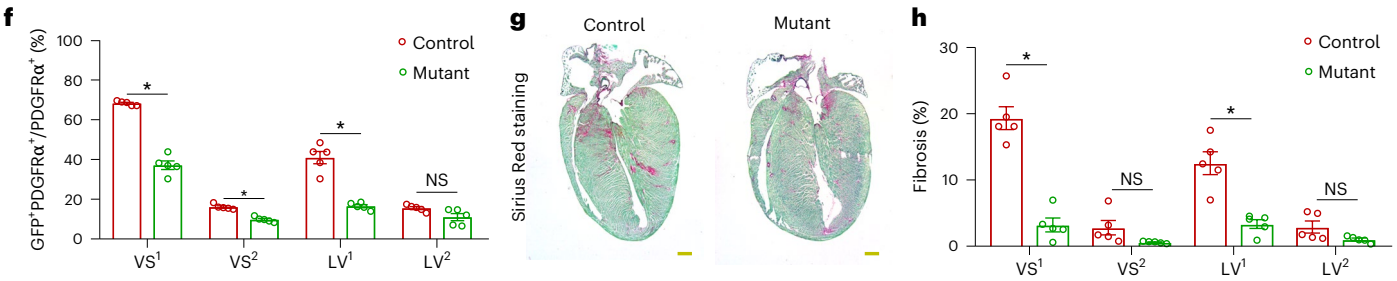

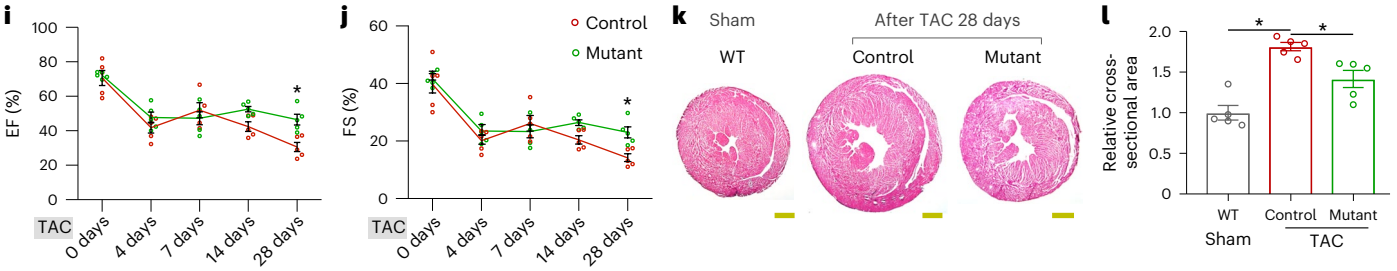

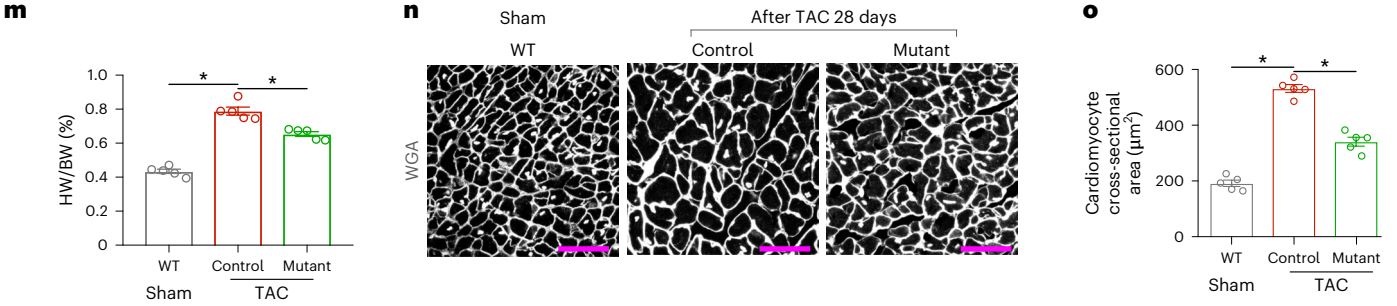

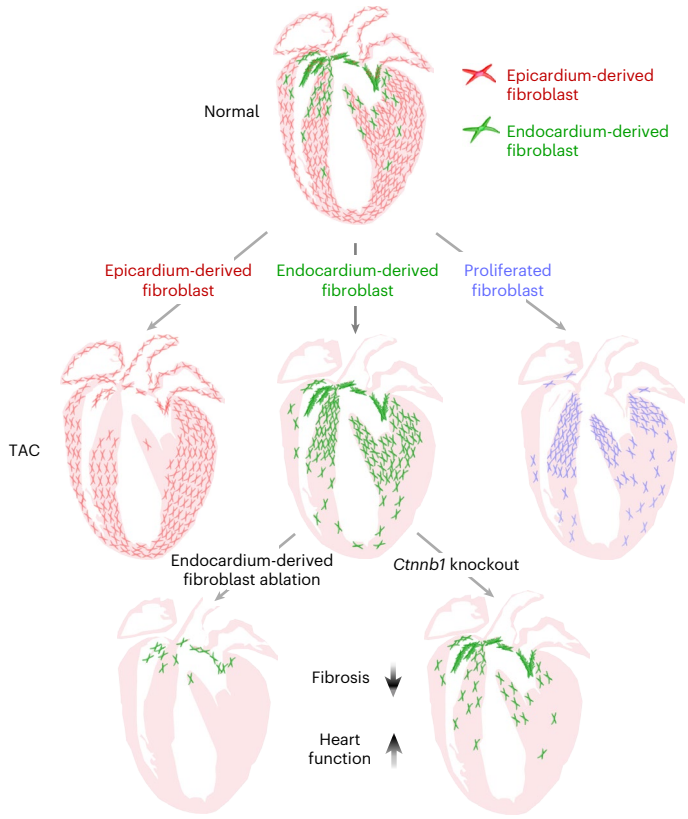

Fig. 8 | Endocardium-derived fibroblasts expand after TAC and targeting them alleviates cardiac fibrosis. Endocardium-derived fibroblasts are distributed regionally in the heart. After TAC-induced injury, a highly regional proliferation of fibroblasts takes place, which is mainly contributed by endocardium-derived fibroblasts. Genetic ablation of endocardium-derived fibroblasts or knockout of the Wnt signaling pathway in endocardium-derived fibroblasts significantly reduces their expansion, ameliorates the severity of cardiac fibrosis and reduces the decline of heart function.

myocardial infarction[40]. In ischemic injury such as myocardial infarction, epicardium-derived fibroblasts may have an important role in driving regional severe fibrosis of the anterior LV wall. Whether relatively few endocardium-derived fibroblast residing in this region could be activated after myocardial infarction and expand significantly in response to ischemic injury is to be addressed in future studies. It would also be interesting to explore whether this unique fibroblast population affects cardiomyocyte proliferation and angiogenesis during cardiac repair and regeneration. Answering these questions with specific genetic tools targeting the heterogeneous subpopulations of fibroblasts would not only provide a better understanding of the pathological program of disease-specific tissue fibrosis but also give new insights into therapeutic development to control the initiation and progression of cardiac diseases such as cardiac fibrosis with an ultimate goal to prevent heart failure.

Online content

Any methods, additional references, Nature Portfolio reporting summaries, source data, extended data, supplementary information, acknowledgements, peer review information; details of author contributions and competing interests; and statements of data and code availability are available at https://doi.org/10.1038/s41588-023-01337-7.

References

1. Wang, W. et al. Global burden of disease study 2019 suggests that metabolic risk factors are the leading drivers of the burden of ischemic heart disease. *Cell Metab.* **33**, 1943–1956 (2021).
2. Tzahor, E. & Poss, K. D. Cardiac regeneration strategies: staying young at heart. *Science* **356**, 1035–1039 (2017).
3. Sadek, H. & Olson, E. N. Toward the goal of human heart regeneration. *Cell Stem Cell* **26**, 7–16 (2020).
4. Bergmann, O. et al. Dynamics of cell generation and turnover in the human heart. *Cell* **161**, 1566–1575 (2015).
5. Pinto, A. R. et al. Revisiting cardiac cellular composition. *Circ. Res.* **118**, 400–409 (2016).
6. Souders, C. A., Bowers, S. L. & Baudino, T. A. Cardiac fibroblast: the renaissance cell. *Circ. Res.* **105**, 1164–1176 (2009).
7. Xie, M., Burchfield, J. S. & Hill, J. A. Pathological ventricular remodeling: therapies: part 2 of 2. *Circulation* **128**, 1021–1030 (2013).
8. Molkentin, J. D. et al. Fibroblast-specific genetic manipulation of p38 mitogen-activated protein kinase in vivo reveals its central regulatory role in fibrosis. *Circulation* **136**, 549–561 (2017).
9. Davis, J. & Molkentin, J. D. Myofibroblasts: trust your heart and let fate decide. *J. Mol. Cell. Cardiol.* **70**, 9–18 (2014).
10. Harris, K. M. et al. Prevalence, clinical profile, and significance of left ventricular remodeling in the end-stage phase of hypertrophic cardiomyopathy. *Circulation* **114**, 216–225 (2006).
11. Bowers, S. L., Banerjee, I. & Baudino, T. A. The extracellular matrix: at the center of it all. *J. Mol. Cell. Cardiol.* **48**, 474–482 (2010).
12. Leask, A. TGFβ, cardiac fibroblasts, and the fibrotic response. *Cardiovasc. Res.* **74**, 207–212 (2007).
13. Rockey, D. C., Bell, P. D. & Hill, J. A. Fibrosis—a common pathway to organ injury and failure. *N. Engl. J. Med.* **372**, 1138–1149 (2015).
14. Li, Y., Lui, K. O. & Zhou, B. Reassessing endothelial-to-mesenchymal transition in cardiovascular diseases. *Nat. Rev. Cardiol.* **15**, 445–456 (2018).
15. Gittenberger-de Groot, A. C., Vrancken Peeters, M. P., Mentink, M. M., Gourdie, R. G. & Poelmann, R. E. Epicardium-derived cells contribute a novel population to the myocardial wall and the atrioventricular cushions. *Circ. Res.* **82**, 1043–1052 (1998).
16. Wilm, B., Ipenberg, A., Hastie, N. D., Burch, J. B. & Bader, D. M. The serosal mesothelium is a major source of smooth muscle cells of the gut vasculature. *Development* **132**, 5317–5328 (2005).
17. Zhou, B. et al. Epicardial progenitors contribute to the cardiomyocyte lineage in the developing heart. *Nature* **454**, 109–113 (2008).
18. Moore-Morris, T. et al. Resident fibroblast lineages mediate pressure overload-induced cardiac fibrosis. *J. Clin. Invest.* **124**, 2921–2934 (2014).
19. Ali, S. R. et al. Developmental heterogeneity of cardiac fibroblasts does not predict pathological proliferation and activation. *Circ. Res.* **115**, 625–635 (2014).
20. Chen, Q. et al. Endothelial cells are progenitors of cardiac pericytes and vascular smooth muscle cells. *Nat. Commun.* **7**, 12422 (2016).
21. Tian, X., Pu, W. T. & Zhou, B. Cellular origin and developmental program of coronary angiogenesis. *Circ. Res.* **116**, 515–530 (2015).
22. Zhang, H. et al. Endocardium contributes to cardiac fat. *Circ. Res.* **118**, 254–265 (2016).
23. Tian, X. et al. Generation of a self-cleaved inducible Cre recombinase for efficient temporal genetic manipulation. *EMBO J.* **39**, e102675 (2020).
24. He, L. et al. Enhancing the precision of genetic lineage tracing using dual recombinases. *Nat. Med.* **23**, 1488–1498 (2017).
25. Zhang, H. et al. Endocardium minimally contributes to coronary endothelium in the embryonic ventricular free walls. *Circ. Res.* **118**, 1880–1893 (2016).
26. Zhang, H. et al. Genetic lineage tracing identifies endocardial origin of liver vasculature. *Nat. Genet.* **48**, 537–543 (2016).

27. Madisen, L. et al. A robust and high-throughput Cre reporting and characterization system for the whole mouse brain. *Nat. Neurosci.* **13**, 133–140 (2010).
28. Fu, X. et al. Specialized fibroblast differentiated states underlie scar formation in the infarcted mouse heart. *J. Clin. Invest.* **128**, 2127–2143 (2018).
29. Kanisicak, O. et al. Genetic lineage tracing defines myofibroblast origin and function in the injured heart. *Nat. Commun.* **7**, 12260 (2016).
30. Bugg, D. et al. MBNL1 drives dynamic transitions between fibroblasts and myofibroblasts in cardiac wound healing. *Cell Stem Cell* **29**, 419–433 (2022).
31. Farbehi, N. et al. Single-cell expression profiling reveals dynamic flux of cardiac stromal, vascular and immune cells in health and injury. *eLife* **8**, e43882 (2019).
32. He, L. et al. Preexisting endothelial cells mediate cardiac neovascularization after injury. *J. Clin. Invest.* **127**, 2968–2981 (2017).
33. Tallquist, M. D. & Molkentin, J. D. Redefining the identity of cardiac fibroblasts. *Nat. Rev. Cardiol.* **14**, 484–491 (2017).
34. He, L. et al. Proliferation tracing reveals regional hepatocyte generation in liver homeostasis and repair. *Science* **371**, eabc4346 (2021).
35. Kaur, H. et al. Targeted ablation of periostin-expressing activated fibroblasts prevents adverse cardiac remodeling in mice. *Circ. Res.* **118**, 1906–1917 (2016).
36. McLellan, M. A. et al. High-resolution transcriptomic profiling of the heart during chronic stress reveals cellular drivers of cardiac fibrosis and hypertrophy. *Circulation* **142**, 1448–1463 (2020).
37. Rinkevich, Y. et al. Skin fibrosis. Identification and isolation of a dermal lineage with intrinsic fibrogenic potential. *Science* **348**, aaa2151 (2015).
38. Aghajanian, H. et al. Targeting cardiac fibrosis with engineered T cells. *Nature* **573**, 430–433 (2019).
39. Rurik, J. G. et al. CAR T cells produced in vivo to treat cardiac injury. *Science* **375**, 91–96 (2022).
40. Zhou, B. et al. Adult mouse epicardium modulates myocardial injury by secreting paracrine factors. *J. Clin. Invest.* **121**, 1894–1904 (2011).

[1]State Key Laboratory of Cell Biology, Shanghai Institute of Biochemistry and Cell Biology, Center for Excellence in Molecular Cell Science, Chinese Academy of Sciences University of the Chinese Academy of Sciences, Shanghai, China. [2]School of Life Science and Technology, ShanghaiTech University, Shanghai, China. [3]Department of Vascular Surgery, Zhongshan Hospital, Fudan University, Shanghai, China. [4]School of Life Sciences, Westlake University, Hangzhou, China. [5]Key Laboratory of Systems Health Science of Zhejiang Province, School of Life Science, Hangzhou Institute for Advanced Study, University of the Chinese Academy of Sciences, Hangzhou, China. [6]Chinese Aacademy of Sciences Key Laboratory of Nutrition, Metabolism and Food Safety, Shanghai Institute of Nutrition and Health, University of the Chinese Academy of Sciences, Chinese Academy of Sciences, Beijing, China. [7]Shanghai Laboratory Animal Research Center, Shanghai, China. [8]Bioscience Cardiovascular, Research and Early Development, Cardiovascular, Renal and Metabolism, BioPharmaceuticals R&D, AstraZeneca, Gothenburg, Sweden. [9]The Collaborative Innovation Center for Cardiovascular Disease Translational Medicine, Nanjing Medical University, Nanjing, China. [10]Division of Cardiology, Department of Medicine, Baylor College of Medicine, Houston, TX, USA. [11]Department of Pediatric Cardiaovascular Surgery, Children's Hospital, School of Medicine, Zhejiang University, National Clinical Research Center for Child Health, Hangzhou, China. [12]Department of Chemical Pathology and Li Ka Shing Institute of Health Sciences, Prince of Wales Hospital, The Chinese University of Hong Kong, Hong Kong, China. [13]Department of Vascular Surgery, Zhongshan Hospital (Xiamen), Fudan University, Xiamen, China. [14]New Cornerstone Science Laboratory, Shenzhen, China. [15]These authors contributed equally: Maoying Han, Zixin Liu, Lei Liu.
✉e-mail: zhoubin@sibs.ac.cn

Methods

Mice

All mice experiments were performed in accordance with the guidelines of the Institutional Animal Care and Use Committee at the Center for Excellence in Molecular Cell Science, Shanghai Institutes of Biological Sciences, Chinese Academy of Science (CAS). The *ACTB-Cre*[24], *CAG-Dre*[24], *Nfatc1-Dre*[22], *Col1a2-CreER*[23], *R26-LSL-tdTomato*[27], *R26-RSR-tdTomato*[25], *Npr3-ZsGreen*[41], *Npr3-DreER*[42], *R26-RSR-ZsGreen*[43], *Wt1-CreER*[17] and *Ctnnb1-flox*[44] mouse lines have been reported previously. The *R26-RL-GFP*, *Ki67-LSL-2A-Dre*, *R26-LSL-RSR-tdT-DTR*, *Npr3-tTA* and *Col1a2-RSR-CreER* mouse lines were generated by homologous recombination using CRISPR–Cas9 technology; the *Tnnt2-Dre-Cre-tdTomato* mouse lines were generated by homologous recombination using the ES cell strategy. In short, a complementary DNA (cDNA) encoding rox-Stop-rox-*loxP*-Stop-*loxP*-GFP-WPRE-poly(A) was inserted between exons 1 and 2 of the endogenous *Rosa26* gene locus to generate the *R26-RL-GFP* mouse line. A cDNA encoding Dre -2A-Cre-2A-tdTomato-WPRE-poly(A) was inserted between the exons 1 and 2 of the *Tnnt2* WT allele to generate the *Tnnt2-Dre-Cre-tdTomato* mouse line. A cDNA encoding rox-Stop-rox-CreER-WPRE-poly(A) was knocked into the *Col1a2* site by homologous recombination to generate the *Col1a2-RSR-CreER* mouse line. A cDNA encoding LSL-RSR-tdTomato-P2A-DTR-WPRE-poly(A) was inserted between exons 1 and 2 of the endogenous *Rosa26* gene locus to generate the *R26-LSL-RSR-tdT-DTR* mouse line. A cDNA encoding LSL-P2A-Dre was inserted into the last coding exon of the *Ki67* gene to generate the *Ki67-LSL-2A-Dre* mouse line. A cDNA encoding tTA-WPRE-poly(A) was inserted into endogenous ATG of *Npr3* by homologous recombination to generate the *Npr3-tTA* mouse line. All mice were maintained under a C57BL6/ICR mixed background and a 12-h light–dark cycle. All mice were fed a normal diet (catalog no. 1010085, Jiangsu Xietong Pharmaceutical Bioengineering). Mice were assigned to different groups randomly in all experiments. The *R26-RL-GFP*, *R26-LSL-RSR-tdT-DTR*, *Tnnt2-Dre-Cre-tdTomato*, *Npr3-tTA* and *Col1a2-RSR-CreER* mouse lines were generated by Shanghai Biomodel Organism. The *Ki67-LSL-2A-Dre* mouse line was generated by Cyagen Biosciences.

TAM and DT treatment

TAM (20 mg ml^{-1} dissolved in corn oil, catalog no. T5648, Sigma-Aldrich) or 4-hydroxy TAM (10 mg ml^{-1} dissolved in absolute ethyl alcohol and corn oil, catalog no. H7904, Sigma-Aldrich) was administered by oral gavage at the assigned time points to induce the activity of CreER in the mouse lines mentioned above. The dose was 0.2 mg g^{-1} body weight each time. For *Nfatc1-Dre;Col1a2-CreER;R26-RL-GFP* mice, a single dose of TAM or 4-hydroxy TAM was administered to pregnant mice at the indicated time points to reveal the biological process at the specific embryonic stages. Adult mice were treated with TAM at 8 weeks old three times consecutively to promote the efficiency of CreER-mediated recombination; TAC was performed in 11-week-old mice. For *Npr3-DreER;R26-RSR-ZsGreen* mice, a single dose of TAM was administered to pregnant mice at E10.5 and mouse hearts were collected at E17.5. For *Wt1-CreER;R26-LSL-tdTomato* mice, a single dose of TAM was administered to pregnant mice at E10.5 and TAC was performed in 8-week-old mice. For *Ki67-LSL-2A-Dre;Col1a2-CreER;R26-RL-GFP* mice, TAM was administered three times consecutively in 8-week-old mice and TAC was performed in 11-week-old mice. For *Nfatc1-Dre;Col1a2-CreER;R26-LSL-RSR-tdT-DTR* mice, TAM was administered five times consecutively to 8-week-old mice to ensure that endocardium-derived fibroblasts were traced by tdTomato efficiently followed by TAC in 11-week-old mice. These mice were injected with DT four times consecutively 1 week after TAC. DT was dissolved in PBS (1 μg μl^{-1}) and each mouse was injected intraperitoneally with DT at a dose of 10 μg g^{-1} to genetically ablate the endocardium-derived fibroblasts. For *Nfatc1-Dre;Col1a2-RSR-CreER;R26-RL-GFP* mice, TAM was administered once in 8-week-old mice and hearts were collected 7 days later. For *Nfatc1-Dre;Col1a2-RSR-CreER;R26-RL-GFP;Ctnnb1-fl* mice, TAM was administered five times consecutively to 8-week-old mice to ensure the knockdown of *Ctnnb1* in endocardium-derived fibroblasts and TAC was performed in 11-week-old mice.

Genomic PCR

Genomic DNA for genotyping was collected from mouse toes, which were lysed using lysis buffer consisting of 5 mM EDTA, 100 mM Tris HCl, pH 7.8, 200 mM NaCl, 0.2% sodium dodecyl sulfate and 100 μg ml^{-1} proteinase K at 55 °C overnight. The products were vibrated by vortex to be completely dissolved in the lysis buffer. DNA was precipitated with the addition of an equal volume of absolute ethyl alcohol; then, the products were centrifuged at 25,000*g* for 3 min. The precipitate was washed with 70% ethanol and the DNA was then dissolved with distilled H_2O. All mice were genotyped with genomic PCR accompanied by their specific primers, which were designed as described previously[45].

Tissue collection and whole-mount fluorescence microscopy

The target tissues were collected from mice with specific genotypes and then washed in cold PBS (catalog no. C10010500BT, Gibco) to remove blood. For mouse hearts, 40 mM KCl in PBS was used to induce diastolic arrest. Next, tissues were fixed with 4% paraformaldehyde (PFA) at 4 °C for 1 h or 30 min, depending on the size of the tissues. After fixing, tissues were washed with cold PBS three times. Tissues were placed with a particular orientation in the Petri dish containing 1% agarose gel with a suitable volume of PBS; the whole-mount brightfield and fluorescence images were then captured using an AxioZoom V16 stereo microscope (ZEISS).

Immunostaining and confocal microscopy

Immunostaining was done according to detailed protocols illustrated previously[46]. Briefly, 30% sucrose was used to dehydrate tissues overnight. After dehydration, tissues were embedded in OCT (Sakura) for 1 h at 4 °C and then frozen at −20 °C. Cryosections (10-μm-thick) were collected from the selected tissues under the matched cutting temperature and stuck on the negatively charged slides. Sections were dried in the fume hood for 1 h at room temperature. The dried sections were washed with PBS three times, each time for 5 min. Afterward, sections were blocked with 2.5% normal donkey serum (Jackson ImmunoResearch) and DAPI (1:1,000, Vector Laboratories) in PBS with Tween 20 (0.2% Triton X-100 in PBS) for at least 30 min at room temperature. Sections were incubated with primary antibodies overnight at 4 °C and then washed with PBS for 5 min three times. Alexa-conjugated secondary antibodies (Invitrogen) were used to incubate the sections for 30 min at room temperature. Sections were washed with PBS three times and then mounted using mounting medium. The antibodies used in this study were: primary antibodies including PDGFRα (1:100, catalog no. AF1062, R&D Systems); GFP (1:500, catalog no. ab6662, Abcam); vimentin (1:100, catalog no. 5741s, Cell Signaling Technology); αSMA (1:100, catalog no. ab5694, Abcam); tdTomato (1:1,000, catalog no. 600-401-379, Rockland); WT1 (1:100, catalog no. sc-393498, Santa Cruz Biotechnology); ZsGreen (1:1,000, catalog no. 632474, Clontech); TNNI3 (1:200, catalog no. ab56357, Abcam); CD31 (1:500, catalog no. 553370, BD Pharmingen); VE-Cad (1:100, catalog no. AF1002, R&D Systems); human HB-EGF (DTR) (1:100, catalog no. AF-259-NA, R&D Systems); WGA (1:1,000, catalog no. W32466, Invitrogen); and β-catenin (1:200, catalog no. 610153, BD Pharmingen). Secondary antibodies included Alexa Fluor 555 donkey anti-rabbit (1:1,000, catalog no. A31572, Invitrogen), Alexa Fluor 488 donkey anti-rabbit (1:1,000, catalog no. A21206, Invitrogen); Alexa Fluor 488 donkey anti-goat (1:1,000, catalog no. A11055, Invitrogen); Alexa Fluor 555 donkey anti-goat (1:1,000, catalog no. A32816, Invitrogen); Alexa Fluor 647 donkey anti-goat (1:1,000, catalog no. A21447, Invitrogen); Alexa Fluor 555 donkey anti-mouse (1:1,000, catalog no. A31570, Invitrogen), horseradish peroxidase donkey anti-rat (1:100, catalog no.

712-035-153, JIR); Cyanine 3 Amplification Reagent (1:1,000, catalog no. NEL744001KT, PerkinElmer); Cyanine 5 Amplification Reagent (1:1,000, catalog no. NEL745001KT, PerkinElmer); Fluorescein Amplification Reagent (1:1,000, catalog no. NEL741001KT, PerkinElmer); and ImmPRESS horse anti-goat (1:1, catalog no. MP-7405, Vector Laboratories). Immunostaining images were obtained by Nikon confocal laser scanning microscope (Nikon A1 or Nikon A1 FLIM).

TAC model

TAC was performed in adult mice as described previously[47]. Briefly, mice were anesthetized with isoflurane (2%) mixed with 0.5–1 l min^{-1} 100% O_2. The respiration of mice was controlled at a rate of about 125–150 times per minute and tidal volume was 0.1–0.3 ml. After several preparation and intubation steps in mice, the thymus and adipose tissue were separated from the aortic arch with forceps under a surgical microscope. A small piece of 6.0 filament was then sutured between the innominate and left carotid arteries and two loose knots were banded around the transverse aorta, while a small piece of blunt needle was deposited in parallel to the transverse aorta. The type of blunt needle was selected according to body weight and sex to fit the size of the aorta. After the two knots were quickly tightened, the needle was quickly pulled out to create a 0.33- to 0.45-mm-diameter constriction. Finally, the skin was closed with a 6.0 prolene suture using a continuous stitch pattern. Mice were allowed to recover on a heating pad until awake. A sham-treated group was set up by opening the chest of mice without banding. TAC was performed after TAM injection for a half month. Hearts were collected after TAC at 4, 7 and 28 days.

EdU incorporation assay

For the EdU (catalog no. A10044, Invitrogen) incorporation experiments, adult mice were injected intraperitoneally with 10 μg g^{-1} EdU 4 h before being killed. Hearts were collected from the mice immediately and fixed in 4% PFA at 4 °C for 1 h and dehydrated in 30% sucrose overnight. Heart tissues were cut into 10-μm-thick slices by cryosection for staining. Sections were stained with GFP, tdTomato and EdU. EdU staining was performed with the Click-iT EdU Alexa 647 Imaging Kit (catalog no. C10340, Thermo Fisher Scientific) according to the manufacturer's instructions[48].

Sirius Red staining

Cardiac fibrosis was assessed using Sirius Red staining, which was performed as described previously[48]. Sections were fixed in 4% PFA for 15 min, washed with PBS for 5 min three times and fixed for 24 h in Bouin solution (9% formaldehyde, 5% acetic acid and 0.9% picric acid). On the second day, sections were washed with tap water and incubated in 0.1% Fast Green (Thermo Fisher Scientific) for 3 min. After incubating, sections were washed with tap water and incubated in 1% acetic acid for 1 min. Sections were washed with distilled H_2O and incubated in 0.1% Sirius Red for 2 min and then washed with distilled H_2O. Afterward, sections were dehydrated in 95% ethanol, 100% ethanol and xylene for 5 min twice and then mounted with the resinous medium. Images were captured on an Olympus microscope (BX53).

H&E staining

The morphology of heart sections was assessed by H&E staining, which was performed as described previously[42]. Sections were soaked in water for 5–10 min to wash off excessive OCT and slides were then incubated in hematoxylin A solution for 8 min to stain the nuclei. Next, slides were washed with running tap water 2–3 times and then clarified in 1% concentrated hydrochloric acid diluted in 70% ethanol for 1 min and washed with tap water 2–3 times. Slides were incubated in 1% ammonia water for 1 min and washed with tap water 2–3 times. Next, slides were incubated with eosin Y solution for 10 s to stain the cytoplasm and then rinsed in 95% ethanol for 10 s. Then, slides were soaked in 100% ethanol for 2 min twice. Finally, slides were dehydrated in xylene for 5 min twice. Images were captured on an Olympus microscope (BX53).

Cardiac fibroblast isolation and FACS

Cardiac fibroblasts were isolated from hearts as described previously[49,50]. The reagents used in cell isolation included PBS, FBS (catalog no. A3161001C, Gibco), HBSS (catalog no. 14025092, Gibco), collagenase IV (catalog no. 17104019, Gibco), dispase (catalog no. 354235, BD BioCoat), DNase I (catalog no. LS002139, Worthington Biochemical Corporation) and DMEM (catalog no. 11965092, Gibco). Before killing mice with CO_2, buffers including washing buffer (PBS with 0.8 mM $CaCl_2$), staining buffer (2% FBS in HBSS) and digestion solution (2 mg ml^{-1} collagenase IV and 1.2 U ml^{-1} dispase in washing buffer) were prepared and put on ice. Once mice were killed, the chest was opened and the heart was perfused with 20 ml washing buffer through the right ventricle to wash out the blood cells. The heart was isolated from the body and placed in a dish that included washing buffer; then, the atria and valves were removed, the ventricle was placed in a 1.5-ml centrifuge tube with digestion solution and the tissues were cut into small pieces. After mincing, the tissues were transferred to a 15-ml centrifuge tube with 3 ml digestion solution and the tube was oscillated at a certain frequency for 25–40 min at 37 °C. Tissue suspensions were blown with straws every 8 min. The cell suspension was filtered with a 70-μm filter into a 50-ml centrifuge tube; then, the filter was rinsed with 3 ml washing buffer to terminate the digestion reaction and the tube was placed into a 4 °C centrifuge at 400*g* for 5 min to obtain the cell precipitate. The cell precipitate was resuspended with 4 ml staining buffer followed by centrifugation at 400*g* for 5 min at 4 °C. Afterward, the cell precipitate was resuspended with 300 μl staining buffer with 1% Fc block (catalog no. 14-0161, eBioscience) and incubated for 5 min at room temperature to block nonspecific antigens on the cell surface. Thereafter, the cell suspension was stained with fluorescence-conjugated antibodies against TER-119 PE-Cy7 (1:200, catalog no. 25-5921, eBioscience), CD45 PE-Cy7 (1:400, 25-0451, eBioscience) and CD140a APC (1:40, catalog no. 562777, BD Pharmingen) (to analyze fibroblasts) or CD31 APC (1:40, catalog no. 17-0311-80, eBioscience) (to analyze endothelial cells) for 30 min at 4 °C. After staining, cells were washed with 10 ml staining buffer to elute excess antibodies and then centrifuged at 400*g* for 5 min at 4 °C to obtain the cell pellets; 2 ml staining buffer with 2 μl DAPI and 2 μl DNase I was used to resuspend the cell pellets. DAPI was used to distinguish dead cells from living cells, which were digested with DNase I to avoid cell adhesion. For the flow cytometry analysis, the Beckman CytoFLEX no. 3 was used. For cell sorting, the collection buffer (2% FBS in DMEM) was prepared to collect the single cells and the Sony MA900 or Beckman MoFlo Astrios EQ was used to sort the cells. Total cell counts were gated first; then, the relative width in forward scatter (FSC) under a certain height in FSC was selected to define the single-cell gate. Next, the $DAPI^-$ cells were gated as live cells. CD45 and TER-119 were used to exclude white and red blood cells, respectively. $PDGFR\alpha^+$ cells were gated as fibroblasts from the $CD45^-TER\text{-}119^-$ gate. Finally, GFP was further defined as GFP^- and GFP^+ fibroblast gates under the $PDGFR\alpha^+$ gate. FACS data were analyzed with FlowJo 10.4 (FlowJo LLC).

RNA extraction

GFP^+ and GFP^- fibroblasts were collected from the same mouse heart by FACS. All samples were suspended with 500 μl TRIzol Reagent (catalog no. 15596018, Invitrogen) and then left to stand for 10 min at room temperature. Next, 100 μl chloroform was added to all samples, which were shaken vigorously manually for 15 s and then incubated in the reagent for 5 min at room temperature. Then, samples were centrifuged at 12,000*g* for 15 min at 4 °C. Between time gaps, 1.5-ml centrifuge tubes were prepared with 250 μl isopropanol. After centrifugation was completed, the upper aqueous phase was carefully pipetted into the tubes prepared as described above and mixed well. Samples were incubated for 10 min at room temperature and then centrifuged at 12,000*g* for

15 min at 4 °C. Then, the supernatant was discarded and supplemented with 1 ml RNA and 75% ethanol to wash the RNA products, followed by centrifugation at 12,000*g* at 4 °C for 5 min. The supernatant was discarded carefully and the RNA products were dried in a fume hood at room temperature for 10 min. Finally, the RNA products were dissolved with a suitable amount of RNase-free water and concentrations were measured with NanoDrop 2000 (Thermo Fisher Scientific).

RNA sequencing and analysis

Total RNA was extracted from the isolated cells using the RNeasy Micro Kit (QIAGEN) according to the manufacturer's instructions. Briefly, cells were treated with an appropriate volume of Buffer RL and one volume of 70% ethanol. The mixture was transferred into an RNeasy MinElute spin column and centrifuged for 15 s at ≥8,000*g*. After the flow-through was discarded, Buffer RW1, DNase I, Buffer RPE and 80% ethanol were added and centrifuged as follows. The RNeasy MinElute spin column, which contained RNA, was placed in a new 2-ml collection tube, centrifuged with the lid open at full speed for 5 min to dry the membrane and then transferred to a new 1.5-ml tube with an appropriate volume of RNase-free water. Finally, tubes were centrifuged for 1 min at full speed to elute the RNA. Total RNA was qualified and quantified using a NanoDrop and Agilent 2100 bioanalyzer (Thermo Fisher Scientific). High-quality RNA was used for messenger RNA library construction. Limited RNA (>200 pg, high-quality) was amplified with oligo(dT) and deoxynucleoside triphosphate, incubated at 72 °C and immediately put back on ice; then, it was reverse-transcribed to cDNA based on the poly(A) tail. The template was switched to the 5′ end of the RNA and the full-length cDNA was generated by PCR. The Agilent 2100 bioanalyzer (Thermo Fisher Scientific) was used to determine the average molecule length of the PCR product. Purified cDNA from the previous steps was fragmented into small pieces with fragment buffer by PCR and the product was purified and selected using the Agencourt AMPure XP-Medium Kit (Thermo Fisher Scientific). cDNA was quantified with the Agilent 2100 bioanalyzer. The double-stranded PCR product undergoing the quality control step was heat-denatured and circularized by the splint oligonucleotide sequence. The single-stranded circular DNA was formatted as the final library. The final library was quantitated in two ways to ensure the high quality of the sequencing data: (1) determination of the average molecule length using the Agilent 2100 bioanalyzer and (2) quantification of the library using RT–qPCR. The final library was amplified with phi29 (Thermo Fisher Scientific) to make DNA nanoballs, which had more than 300 copies of one molecule. DNA nanoballs were loaded into the patterned nanoarray and single-end 50-bp reads were generated on the MGISEQ-2000RS platform (BGI-Shenzhen). The filtered reads were aligned against the Ensembl mouse genome version mm10 (GRCm38) using HISAT2 v.0.1.6-beta with default parameters. The number of reads aligning to genes was counted with HTSeq v.2.0.1. Only reads mapping at least partially inside exons were allowed and aggregated per gene. Reads overlapping multiple genes or aligning to multiple regions were excluded. Analysis of DEGs was performed using DESeq2 v.1.34.0. GSEA was performed on GSEA v.4.0.3 (Broad Institute). GO enrichment analysis was performed on the clusterProfiler R package v.4.2.2.

Statistical analysis

Data are displayed as the mean ± s.e.m. of at least three biological duplicates performed individually under the same conditions. For each mouse heart, we collected 8–16 heart sections for immunostaining; from each section, we took 3–5 fields for quantification. The researcher who quantified the fluorescence staining images was blinded to the groups of mice. A two-way ANOVA with Šidák's multiple comparisons test was used to correct either the alpha or *P* value of a range of hypotheses to control the family-wise error rate in Figs. 2j, 5e,g,i and 7f,h–j, Extended Data Fig. 7e and Supplementary Figs. 6f, 7f, 10 and 11. A two-way ANOVA with Tukey's multiple comparisons test was used to compare the means of multiple groups in Fig. 4i, Extended Data Fig. 4g and Supplementary Fig. 5e. A one-way ANOVA with Tukey's multiple comparisons test was used in Figs. 5k,l,n and 7l,m,o and Supplementary Fig. 2i. An unpaired Student's *t*-test was performed in Fig. 7c, Extended Data Figs. 1f, 7g–i and 10b–d and Supplementary Fig. 8f. A Wald test was performed in Fig. 6c,h,i. An overrepresentation test was used in Extended Data Fig. 8d. *P* values are provided in each figure panel.

Reporting summary

Further information on research design is available in the Nature Portfolio Reporting Summary linked to this article.

Data availability

The raw sequencing data reported in this study can be accessed at the NCBI Sequence Read Archive under BioProject no. PRJNA813322.

Code availability

This study did not generate any unique code or algorithm. The algorithms used for the analysis in this study are all publicly available. The code used for single-cell data processing and analysis has been deposited in Zenodo (https://doi.org/10.5281/zenodo.7593543).

References

41. Liu, K. et al. Lineage tracing clarifies the cellular origin of tissue-resident macrophages in the developing heart. *J. Cell Biol.* **221**, e202108093 (2022).
42. Han, X. et al. A suite of new Dre recombinase drivers markedly expands the ability to perform intersectional genetic targeting. *Cell Stem Cell* **28**, 1160–1176 (2021).
43. Liu, K. et al. Triple-cell lineage tracing by a dual reporter on a single allele. *J. Biol. Chem.* **295**, 690–700 (2020).
44. Huelsken, J., Vogel, R., Erdmann, B., Cotsarelis, G. & Birchmeier, W. β-Catenin controls hair follicle morphogenesis and stem cell differentiation in the skin. *Cell* **105**, 533–545 (2001).
45. Tian, X. et al. Subepicardial endothelial cells invade the embryonic ventricle wall to form coronary arteries. *Cell Res.* **23**, 1075–1090 (2013).
46. Li, Y. et al. Genetic lineage tracing of non-myocyte population by dual recombinases. *Circulation* **138**, 793–805 (2018).
47. Tang, J. et al. Genetic fate mapping defines the vascular potential of endocardial cells in the adult heart. *Circ. Res.* **122**, 984–993 (2018).
48. Pu, W. et al. Mfsd2a^{+} hepatocytes repopulate the liver during injury and regeneration. *Nat. Commun.* **7**, 13369 (2016).
49. Skelly, D. A. et al. Single-cell transcriptional profiling reveals cellular diversity and intercommunication in the mouse heart. *Cell Rep.* **22**, 600–610 (2018).
50. Zhang, S. et al. Seamless genetic recording of transiently activated mesenchymal gene expression in endothelial cells during cardiac fibrosis. *Circulation* **144**, 2004–2020 (2021).

Acknowledgements

This study was supported by the National Key Research & Development Program of China (grant nos. 2019YFA0110403 and 2019YFA0802000 to B.Z., grant no. 2022YFA1104200 to Y.L. and grant nos. 2021YFA0805100 and 2018YFA0108100 to L.H.), National Science Foundation of China (grant nos. 82088101 and 32050087 to B.Z., grant nos. 82270415 and 81970412 to L.W. and grant no. 32170848 to Y.L.), Shanghai Pilot Program for Basic Research-CAS, Shanghai Branch (grant no. JCYJ-SHFY-2021-0 to B.Z.), CAS Project for Young Scientists in Basic Research (grant no. YSBR-012 to B.Z.), the Pearl River Talent Recruitment Program of Guangdong Province (grant no. 2017ZT07S347 to B.Z.), Young Elite Scientists Sponsorship Program Grant of CAS (to W.P. and Y.L.), Research Grants Council of Hong Kong (grant no. RFS2223-4S04 to K.O.L.), Research Funds of Hangzhou Institute for Advanced Study (grant no. 2022ZZ01015 to X. Li),

Collaborative Innovation Program of Shanghai Municipal Health Commission (grant no. 2020CXJQ01 to B.Z.), Program of Shanghai Academic Research Leader (grant no. 22XD1403700 to B.Z.), the XPLORER PRIZE (to B.Z.), the New Cornerstone Science Foundation (to B.Z.), Shanghai Youth Science and Technology Rising-Star Program (to Y.L.), AstraZeneca, Boehringer Ingelheim and Sanofi-Shanghai Institutes for Biological Sciences Fellowship. We also thank Shanghai Model Organisms Center and Cyagen Biosciences for generating the mice; members of the animal facility and cell platform in Center for Excellence in Molecular Cell Science (CEMCS) and National Center for Protein Science Shanghai for assistance in microscopy; and the Genome Tagging Project Center, CEMCS, CAS for technical support.

Author contributions

M.H. and B.Z. conceived and designed the project. Z.L. performed the RNA sequencing experiments and analysis. L.L., X.H., H.W., W.P., E.W., X. Liu, Y.L., L.H., X. Li, J.W., L.Q., R.S., Q.-D.W., Y.J., R.A., Q.S. and L.W. bred the mice, performed the experiments, analyzed the data or made intellectual contributions to the study. K.O.L. and B.Z. drafted and revised the paper.

Competing interests

The authors declare no competing interests.

Additional information

Extended data is available for this paper at https://doi.org/10.1038/s41588-023-01337-7.

Supplementary information The online version contains supplementary material available at https://doi.org/10.1038/s41588-023-01337-7.

Correspondence and requests for materials should be addressed to Bin Zhou.

Peer review information *Nature Genetics* thanks Xing Fu and the other, anonymous, reviewer(s) for their contribution to the peer review of this work.

https://doi.org/10.1038/s41588-023-01337-7

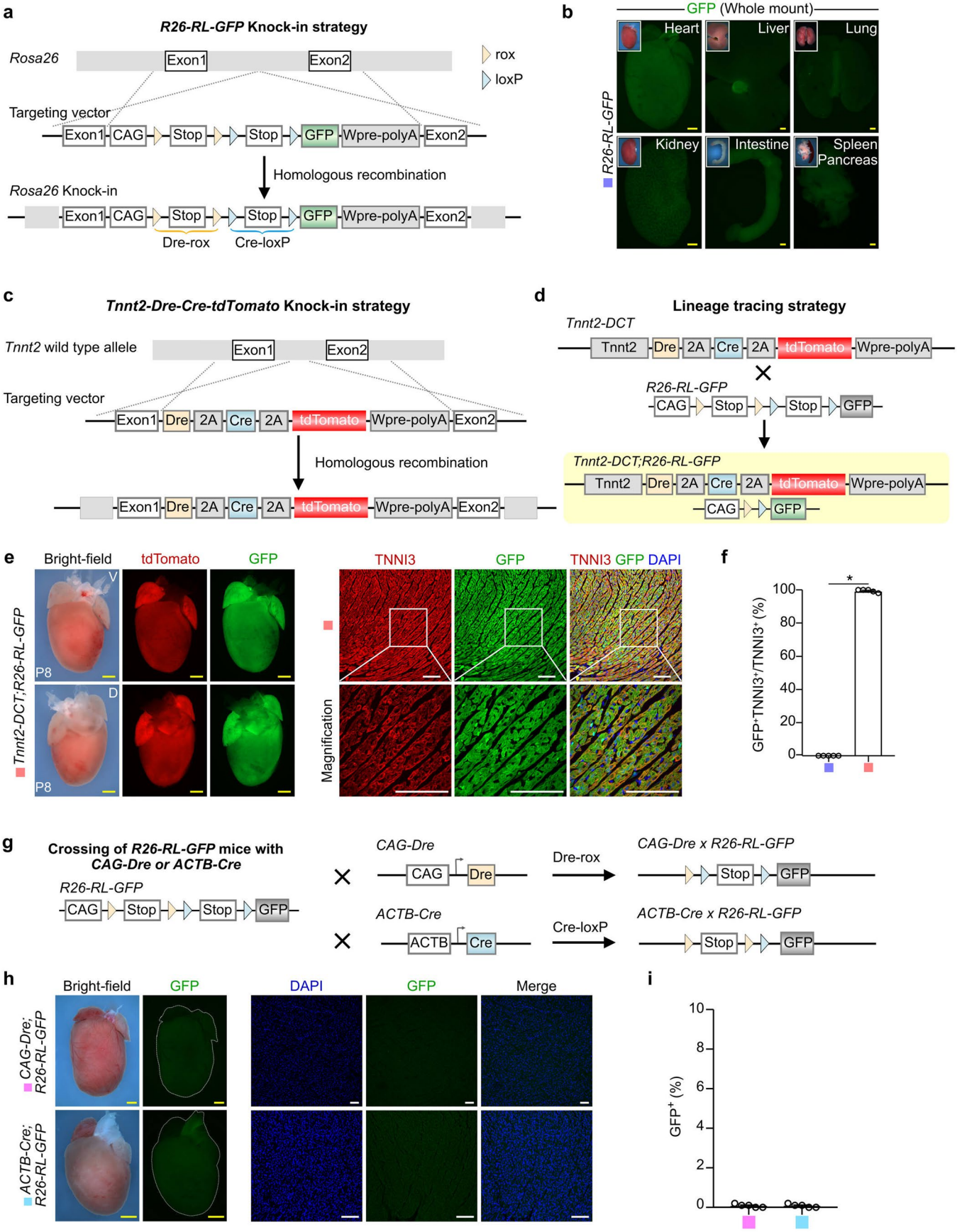

Extended Data Fig. 1 | See next page for caption.

https://doi.org/10.1038/s41588-023-01337-7

Extended Data Fig. 1 | Generation and characterization of *R26-RL-GFP* mouse line. a, Schematic figure showing the knock-in strategy for *R26-RL-GFP* by homologous recombination using CRISPR/Cas9. **b**, Whole-mount bright-field and epifluorescence images of multiple organs collected from adult *R26-RL-GFP* mouse. **c**, Schematic figure showing the knock-in strategy of *Tnnt2-Dre-Cre-tdTomato* (*Tnnt2-DCT*) by homologous recombination. **d**, Schematic diagram showing the Cre-loxP and Dre-rox recombinations after crossing *R26-RL-GFP* with *Tnnt2-DCT* mice. **e**, Whole-mount bright-field and epifluorescence images of *Tnnt2-DCT;R26-RL-GFP* mouse heart (left panel). Immunostaining for TNNI3 and GFP on heart sections (right panel). **f**, Quantification of the percentage of $TNNI3^+$ cardiomyocytes expressing GFP on *Tnnt2-DCT;R26-RL-GFP* heart sections. Data are mean ± s.e.m.; $n = 5$ mice; $^*P < 0.0001$. Statistical analysis was performed by unpaired Student's *t*-test. **g**, Schematic diagram showing the Dre-rox or Cre-loxP recombinations after crossing *R26-RL-GFP* with *CAG-Dre* or *ACTB-Cre*. **h**, Whole mount bright-field and epifluorescence images of *CAG-Dre;R26-RL-GFP* and *ACTB-Cre;R26-RL-GFP* mouse heart (left panel). Immunostaining for GFP on heart sections (right panel). **i**, Quantification of the percentage of GFP^+ cells on mouse heart sections. Data are mean ± s.e.m.; $n = 5$ mice. V, ventricle; D, dorsal. Scale bars, yellow, 1 mm; white, 100 µm. Each image is representative of five individual mouse samples.

https://doi.org/10.1038/s41588-023-01337-7

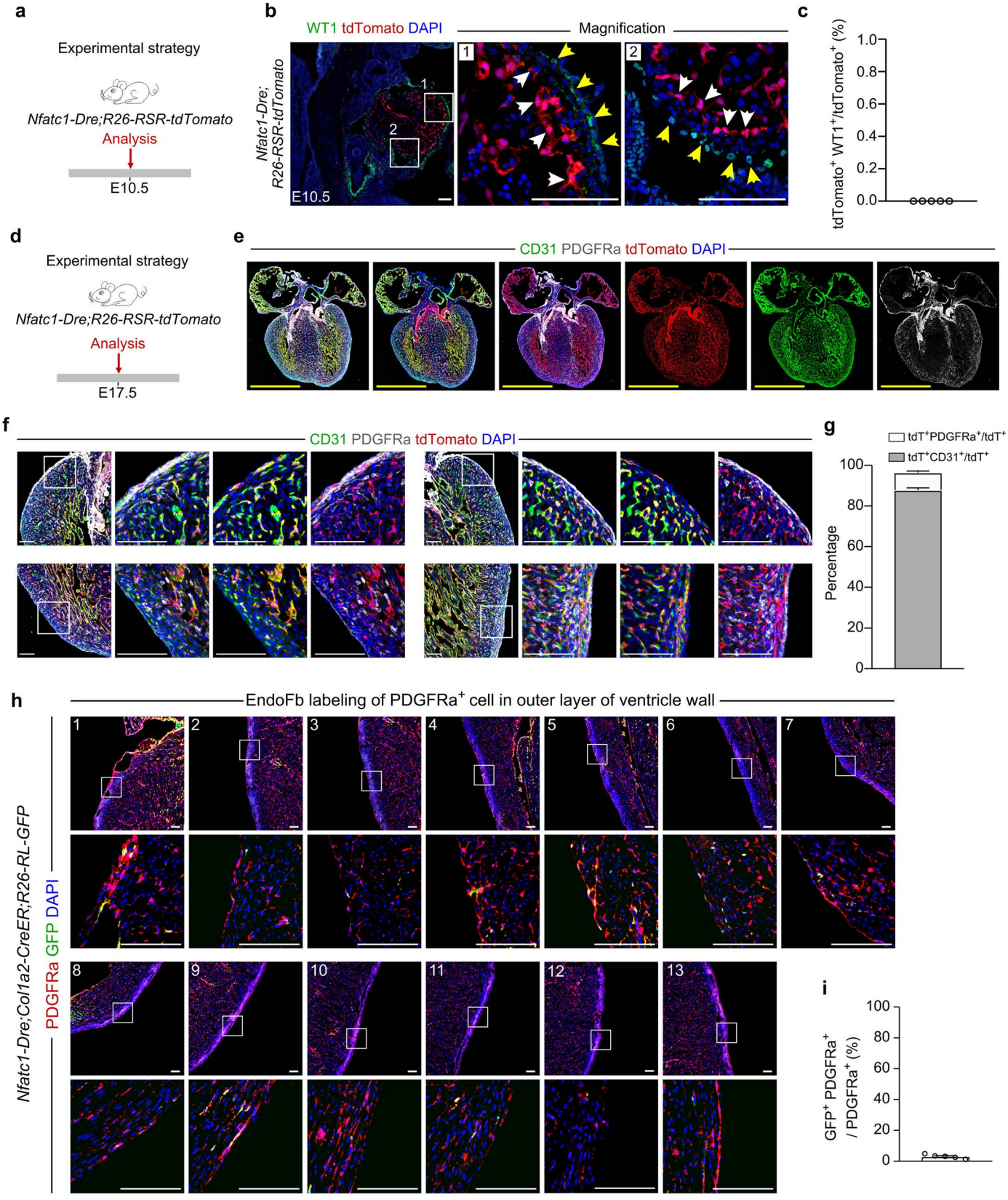

Extended Data Fig. 2 | See next page for caption.

https://doi.org/10.1038/s41588-023-01337-7

Extended Data Fig. 2 | Labeling of cardiac cells by *Nfatc1-Dre*. **a**, Schematic figure showing the experimental strategy. **b**, Immunostaining for WT1 and tdTomato on embryo sections collected from *Nfatc1-Dre;R26-RSR-tdTomato* mice. The boxed areas are magnified on the right panel with split channels. Arrowheads: white, tdTomato$^+$ cells; yellow, WT1$^+$ epicardium cells. **c**, Quantification of the percentage of tdTomato$^+$ cells expressing WT1. Data are mean ± s.e.m.; $n = 5$ mice. **d**, Schematic figure showing the experimental strategy. **e**,**f**, Immunostaining for CD31, PDGFRa, and tdTomato on embryonic sections collected from *Nfatc1-Dre;R26-RSR-tdTomato* mice. **g**, Quantification of the percentage of tdTomato$^+$ cells expressing PDGFRa or CD31 on the outer layer of hearts collected from *Nfatc1-Dre;R26-RSR-tdTomato* mice. Data are mean ± s.e.m.; $n = 5$ mice **h**, Immunostaining for PDGFRa and GFP on adult heart sections collected from *Nfatc1-Dre;Col1a2-CreER;R26-RL-GFP* mice. The boxed areas are magnified on the lower panels. **i**, Quantification of the percentage of PDGFRa$^+$ cells expressing GFP of the outer layer of hearts. Data are mean ± s.e.m.; $n = 5$ mice. Scale bars, yellow, 1 mm, white, 100 µm. Each image is representative of five individual mouse samples.

https://doi.org/10.1038/s41588-023-01337-7

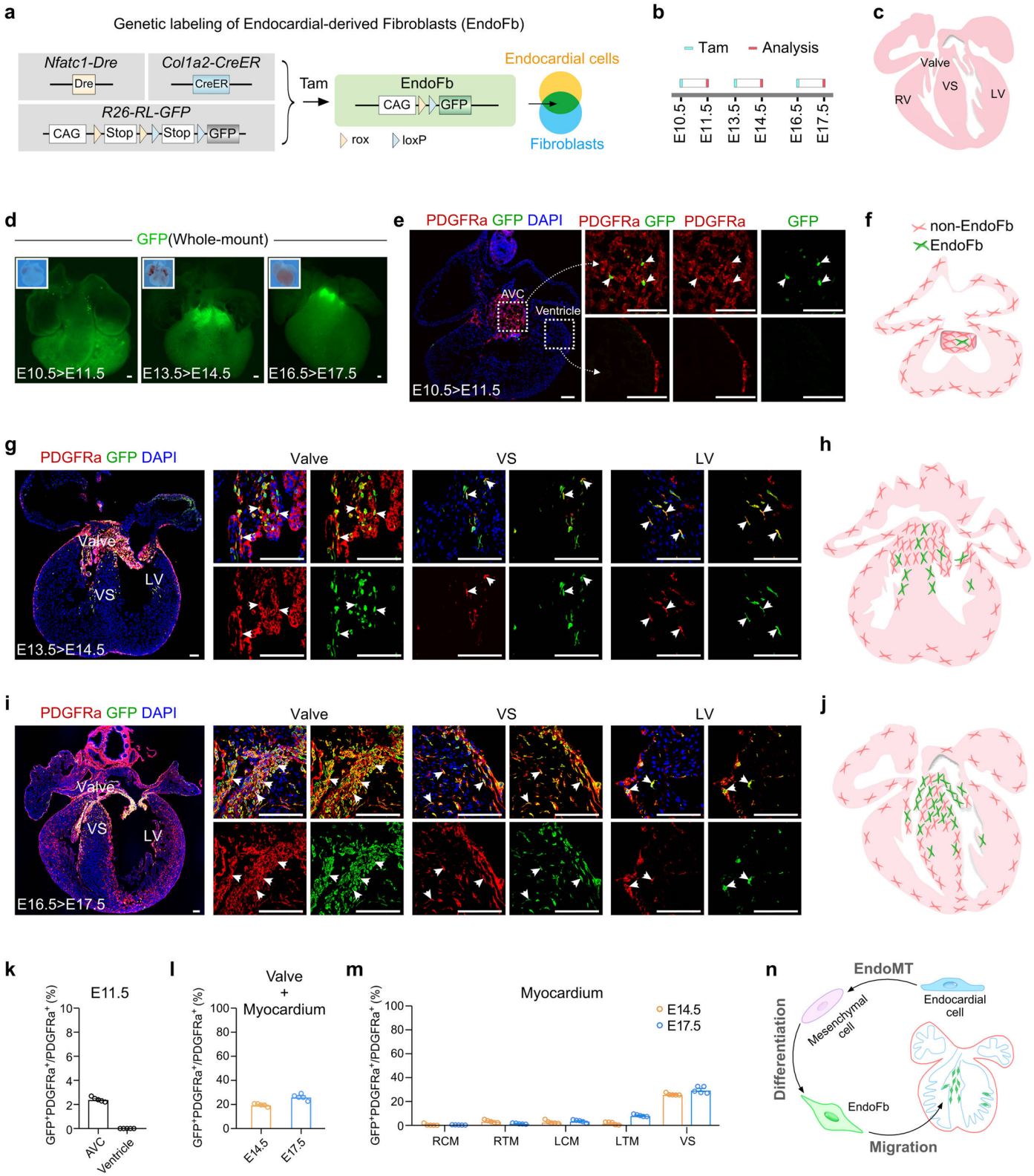

Extended Data Fig. 3 | See next page for caption.

https://doi.org/10.1038/s41588-023-01337-7

Extended Data Fig. 3 | Genetic labeling of endocardium-derived fibroblasts (EndoFb) in developing heart. a, Illustration of the intersectional genetic approach for genetic labeling of EndoFb. **b**, Schematic figure showing the strategy for labelling the EndoFb by tamoxifen (Tam) treatment. **c**, Cartoon image showing different region of embryonic heart. RV, right ventricle; VS, ventricular septum; LV, left ventricle. **d**, Whole-mount (inset) and epifluorescence images of hearts at different embryonic stages show the expression pattern of EndoFb. **e**,**g**,**i**, Immunostaining for PDGFRa and GFP on heart sections of different embryonic stages. The boxed areas are magnified on the right panels with split channels. Arrowheads, $GFP^+PDGFRa^+$ EndoFb. **f**,**h**,**j**, Cartoon images showed the distribution of EndoFb in hearts at different embryonic stages. **k**, Quantification of the percentage of $PDGFRa^+$ fibroblasts expressing GFP in E11.5 hearts. Data are mean ± s.e.m.; $n = 5$ mice. **l**,**m**, Quantification of the percentage for $PDGFRa^+$ EndoFb expressing GFP in E14.5 and E17.5 hearts. Data are mean ± s.e.m.; $n = 5$ mice. RCM, right compact myocardium; RTM, right trabecular myocardium; LCM, left compact myocardium; LTM, left trabecular myocardium; VS, ventricular septum. **n**, Cartoon image showed EndoFb from EndoMT and their subsequent migration into some regions of embryonic hearts. Scale bars, 100 μm. Each image is representative of five individual mouse samples.

https://doi.org/10.1038/s41588-023-01337-7

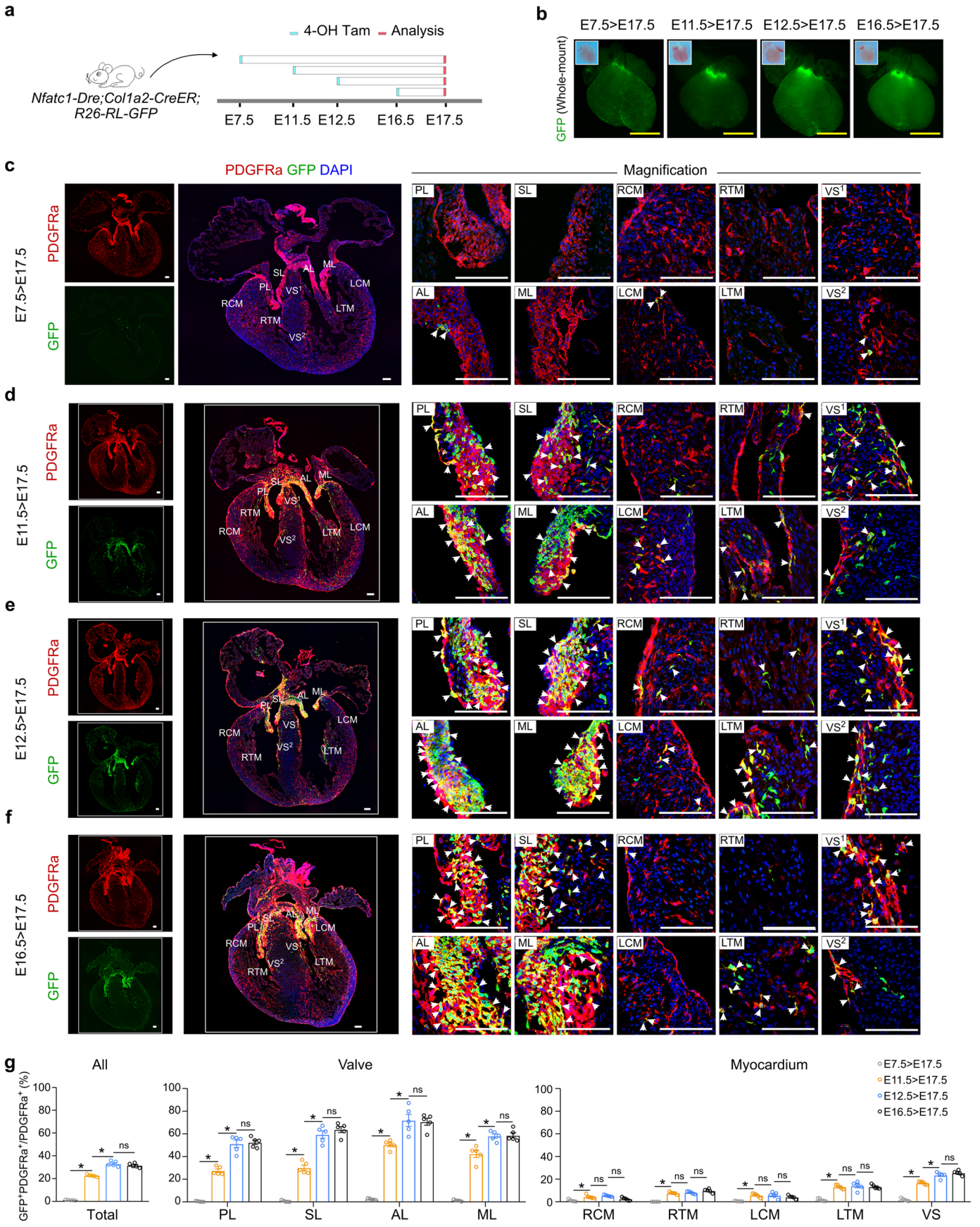

Extended Data Fig. 4 | See next page for caption.

https://doi.org/10.1038/s41588-023-01337-7

Extended Data Fig. 4 | Temporospatial determination of EndoFb fate in developing heart. a, Schematic diagram showing the strategy for labelling the EndoFb in different time window. 4-Hydroxytamoxifen (4-OH Tam) was injected at E7.5, E11.5, E12.5, and E16.5, then collected at E17.5. **b**, Whole-mount and epifluorescence images of E17.5 hearts with Tam induced at different time points. **c-f**, Immunostaining for PDGFRa and GFP on E17.5 heart sections when 4-OH Tam was injected at E7.5, E11.5, E12.5, and E16.5 respectively. Arrowheads, $GFP^+PDGFRa^+$ EndoFb. **g**, Quantification of the percentage of GFP^+ EndoFb expressing PDGFRa in total (left panel), different valves (middle panel), and different regions of ventricles (right panel) in different time window. Data are mean ± s.e.m., $n = 5$ mice. Two-way ANOVA followed by Tukey's multiple comparisons test was used to compare among means of multiple groups. In All, E7.5 > E17.5 vs. E11.5 > E17.5 and E11.5 > E17.5 vs. E12.5 > E17.5, $^*P < 0.0001$. In Valve, PL: E7.5 > E17.5 vs. E11.5 > E17.5 and E11.5 > E17.5 vs. E12.5 > E17.5, $^*P < 0.0001$; SL: E7.5 > E17.5 vs. E11.5 > E17.5 and E11.5 > E17.5 vs. E12.5 > E17.5, $^*P < 0.0001$; AL: E7.5 > E17.5 vs. E11.5 > E17.5 and E11.5 > E17.5 vs. E12.5 > E17.5, $^*P < 0.0001$; ML: E7.5 > E17.5 vs. E11.5 > E17.5, $^*P < 0.0001$; E11.5 > E17.5 vs. E12.5 > E17.5, $^*P = 0.0002$. In Myocardium, RCM: E7.5 > E17.5 vs. E11.5 > E17.5, $^*P = 0.0226$; RTM: E7.5 > E17.5 vs. E11.5 > E17.5, $^*P < 0.0001$; LCM: E7.5 > E17.5 vs. E11.5 > E17.5, $^*P < 0.0001$; LTM: E7.5 > E17.5 vs. E11.5 > E17.5, $^*P < 0.0001$; VS: E7.5 > E17.5 vs. E11.5 > E17.5 and E11.5 > E17.5 vs. E12.5 > E17.5, $^*P < 0.0001$; ns, no significance. PL, parietal leaflet; SL, septal leaflet; AL, aortic valve; ML, mural valve; RCM, right compact myocardium; RTM, right trabecular myocardium; LCM, left compact myocardium; LTM, left trabecular myocardium; VS, ventricular septum. Scale bars: yellow, 200 μm; white, 100 μm. Each image is representative of five individual mouse samples.

https://doi.org/10.1038/s41588-023-01337-7

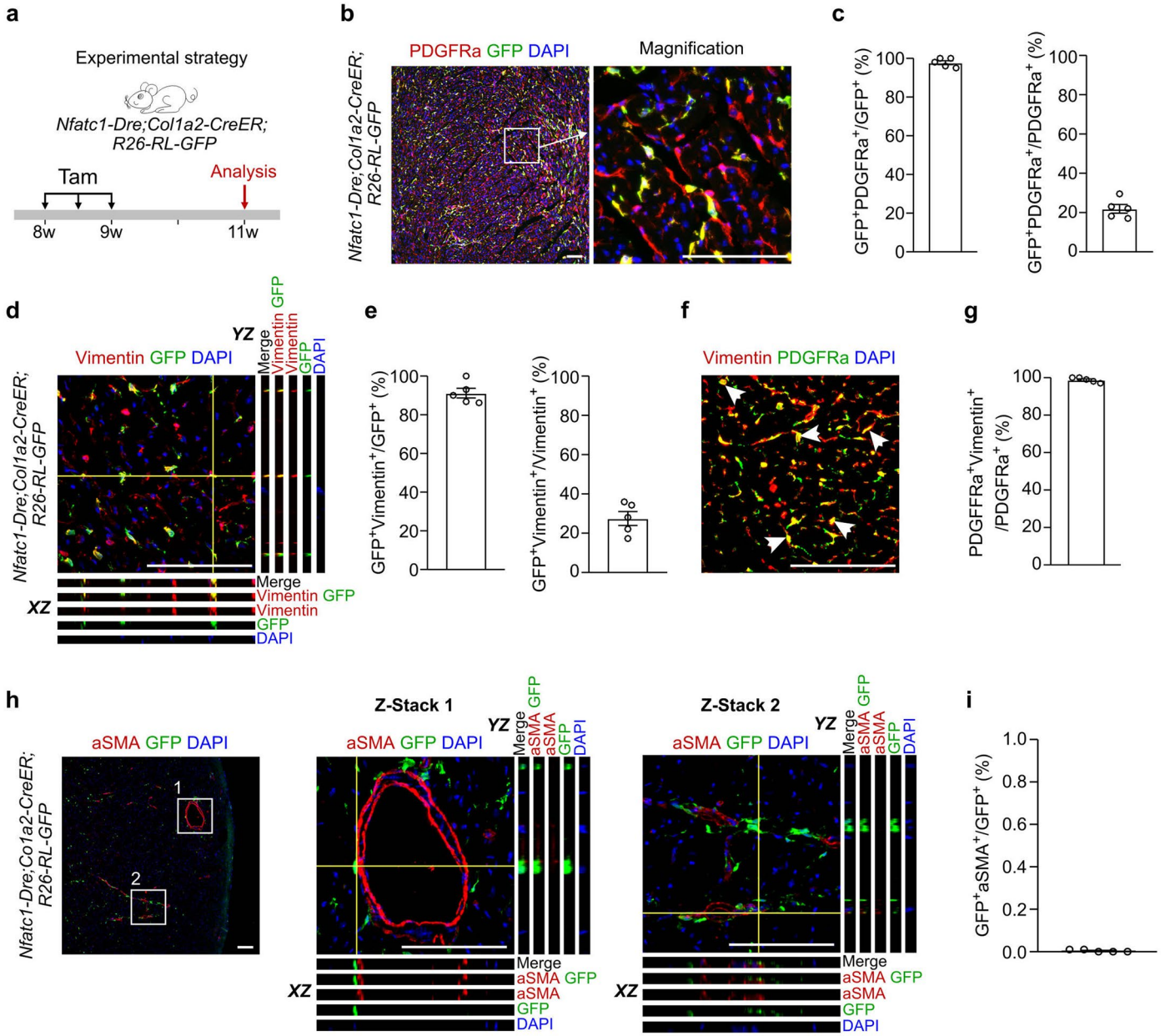

Extended Data Fig. 5 | Expression of fibroblast markers in GFP⁺ EndoFb. **a**, Schematic diagram showing the strategy for labelling the EndoFb. **b**, Immunostaining for PDGFRa and GFP on *Nfatc1-Dre;Col1a2-CreER;R26-RL-GFP* heart sections. The boxed area was magnified on the right panel. **c**, Quantification of the percentage of GFP⁺ cells expressing PDGFRa (left panel), and the percentage of PDGFRa⁺ cells expressing GFP (right panel). **d**, Z-stack confocal images of heart sections stained for Vimentin and GFP. *YZ* and *XZ* indicated signals from dotted lines on Z-stack images. **e**, Quantification of the percentage of GFP⁺ cells expressing Vimentin (left panel) and the percentage of Vimentin⁺ cells expressing GFP (right panel). **f**, Immunostaining for Vimentin and PDGFRa on heart sections. **g**, Quantification of the percentage of PDGFRa⁺ cells expressing Vimentin. **h**, Immunostaining for aSMA and GFP on heart sections. The boxed areas were magnified on the right panel. *YZ* and *XZ* indicated signals from dotted lines on Z-stack images. **i**, Quantification of the percentage of GFP⁺ cells expressing aSMA. Scale bars, 100 μm. All quantification data are represented as mean ± s.e.m.; $n = 5$ mice. Each image is representative of five individual mouse samples.

https://doi.org/10.1038/s41588-023-01337-7

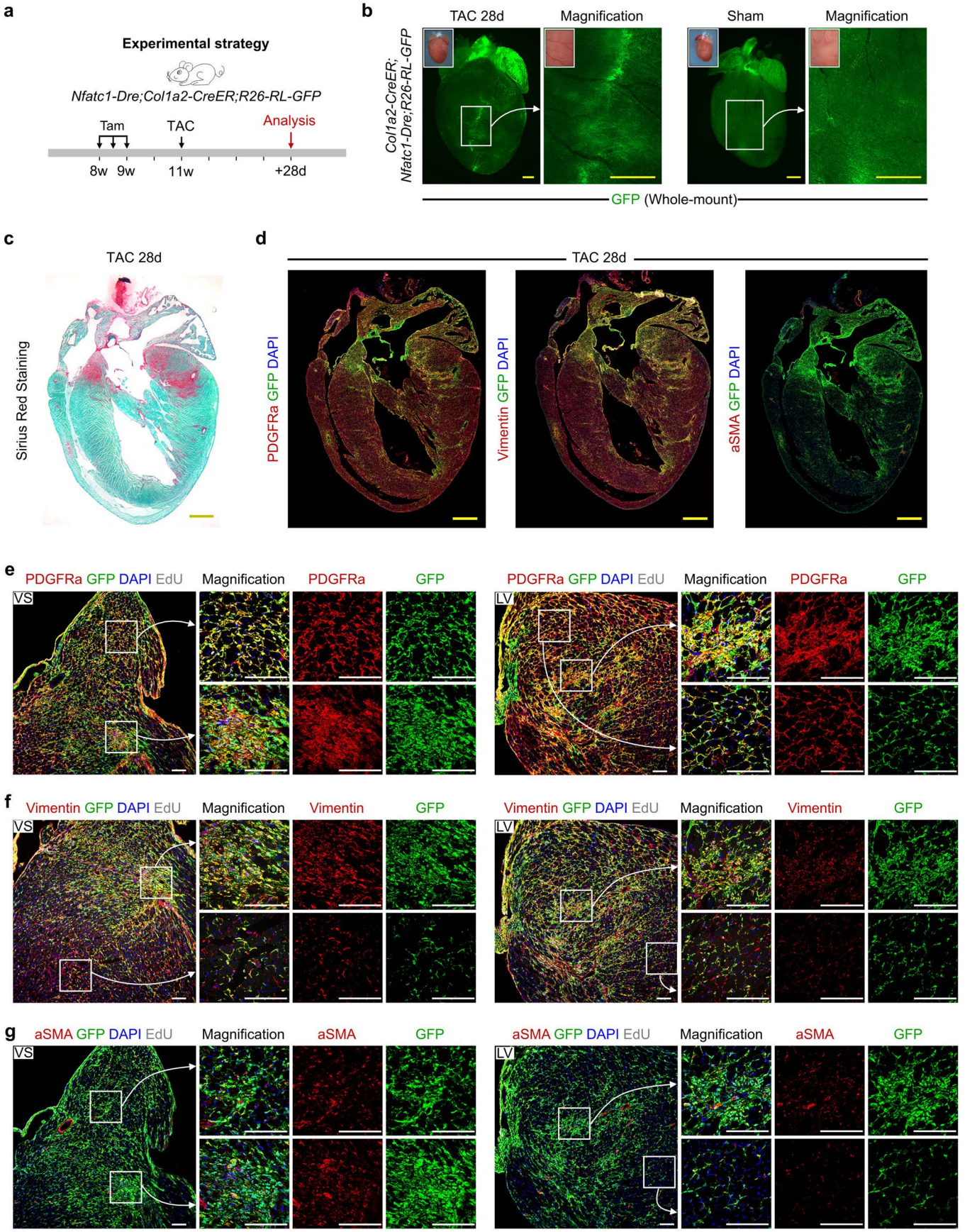

Extended Data Fig. 6 | See next page for caption.

https://doi.org/10.1038/s41588-023-01337-7

Extended Data Fig. 6 | Distribution of EndoFb in hearts at 28 days post TAC. **a**, Schematic diagram showing the experimental strategy. **b**, Whole-mount bright-field and fluorescent views of hearts collected from *Nfatc1-Dre;Col1a2-CreER;R26-RL-GFP* mice at 28d post sham or TAC. **c**, Sirius Red staining images showing the fibrotic area on heart sections collected from mice post TAC 28 days. **d**, Immunostaining for PDGFRa, Vimentin, aSMA, and GFP on whole heart sections. **e**-**g**, Immunostaining for PDGFRa (**e**), Vimentin (**f**), aSMA (**g**), with EdU and GFP on VS and LV of the heart sections. Scale bars: yellow, 1 mm; white, 100 μm. Each image is representative of five individual mouse samples.

https://doi.org/10.1038/s41588-023-01337-7

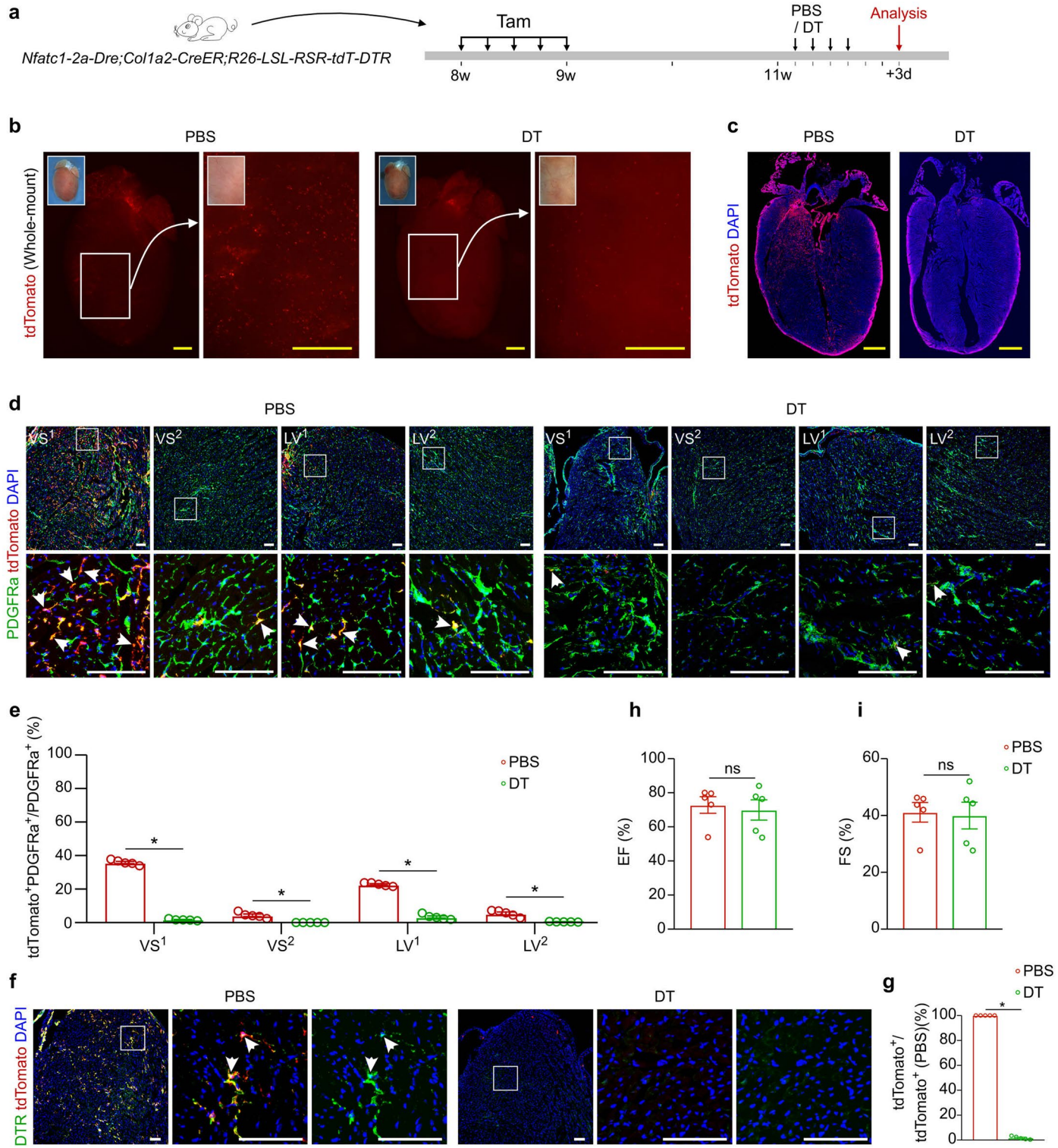

Extended Data Fig. 7 | Efficient genetic ablation of EndoFb. a, Schematic diagram showing the experimental strategy. **b**, Whole-mount bright-field and fluorescent views of hearts collected from mice after PBS- or DT-treatment. **c**, Immunostaining for tdTomato on whole heart sections collected from mice with PBS- or DT-treatment. **d**, Immunostaining for tdTomato and PDGFRa on the different parts of the heart sections collected from mice with PBS- or DT-treatment. **e**, Quantification of the PDGFRa$^+$ fibroblasts expressing tdTomato in different areas of hearts collected from mice treated with PBS or DT. Data are mean ± s.e.m.; $n = 5$ mice; in every area, PBS vs. DT, $^*P < 0.0001$. **f**, Immuostaining for DTR and tdTomato on hearts collected from mice treated with PBS or DT. **g**, Quantification of the percentage of the tdTomato$^+$ cells of hearts collected from mice treated with PBS or DT. Data are mean ± s.e.m.; $n = 5$ mice; $^*P < 0.0001$. **h,i**, Quantification of ejection fraction (EF) and fractional shortening (FS) of mice treated with PBS or DT. Data are mean ± s.e.m.; $n = 5$ mice; ns, no significance. Scale bars: yellow, 1 mm; white, 100 μm. Each image is representative of five individual mouse samples. Two-way ANOVA followed by Sidak's multiple-comparisons test was used in **e**. Unpaired Student's *t*-test was performed in **g-i**.

https://doi.org/10.1038/s41588-023-01337-7

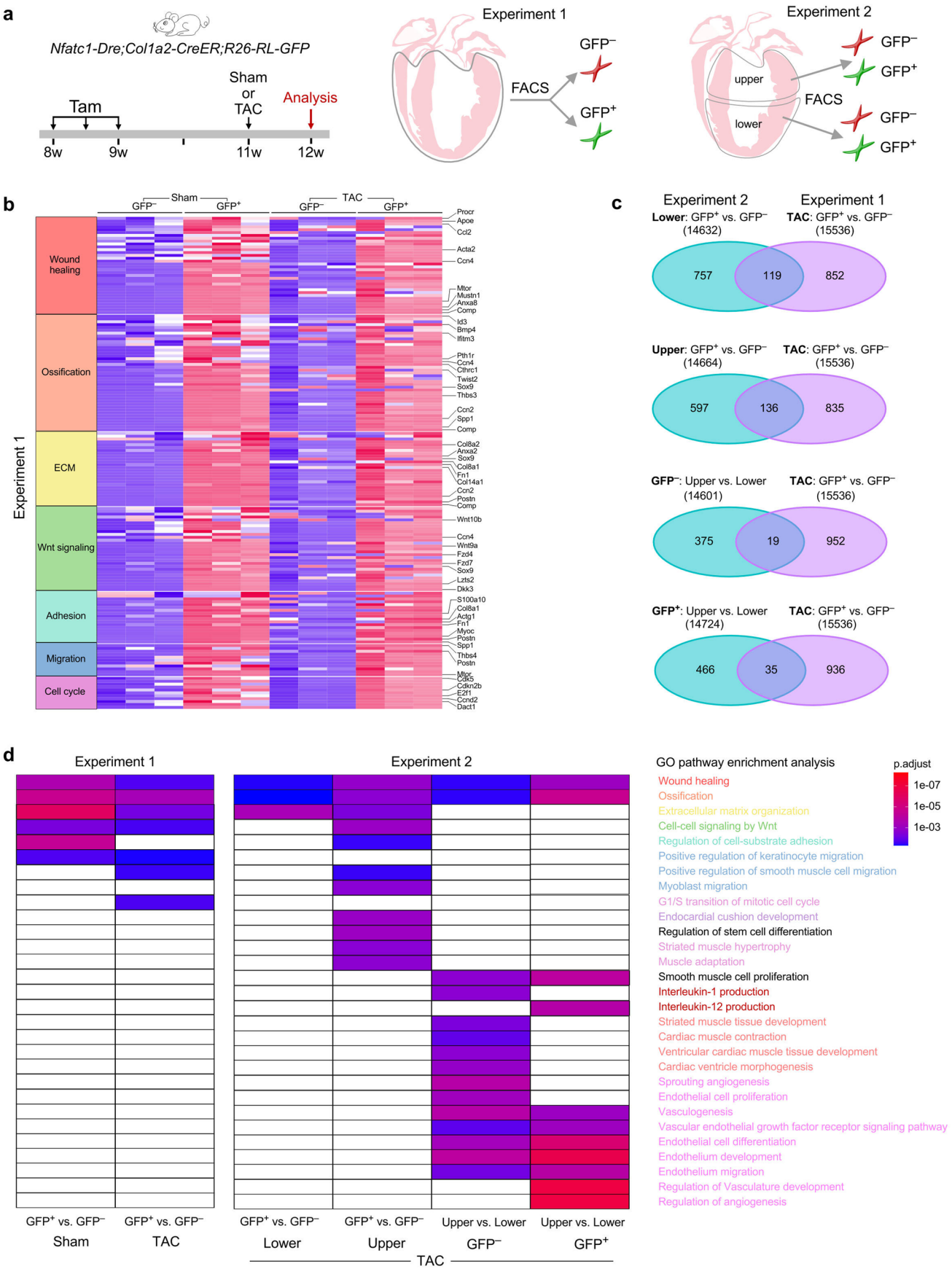

Extended Data Fig. 8 | See next page for caption.

https://doi.org/10.1038/s41588-023-01337-7

Extended Data Fig. 8 | Gene profile of EndoFb and EpiFb after injury. a, Schematic diagram showing two experimental designs. **b**, Gene expression heatmap showing the scaled expression of selected GO pathway-related genes in GFP^+ and GFP^- fibroblasts from Sham or TAC hearts (Experiment 1). **c**, Venn plots showing the number of shared significantly up-regulated genes between the comparison groups from Experiment 1 and 2. **d**, GO pathway enrichment analysis. Each row represents a GO term, and each column represents a comparison group. White cell denotes that gene changes are not enriched in this GO pathway between the comparison groups. Over-representation test was used in **d**; $n = 3$ mice.

https://doi.org/10.1038/s41588-023-01337-7

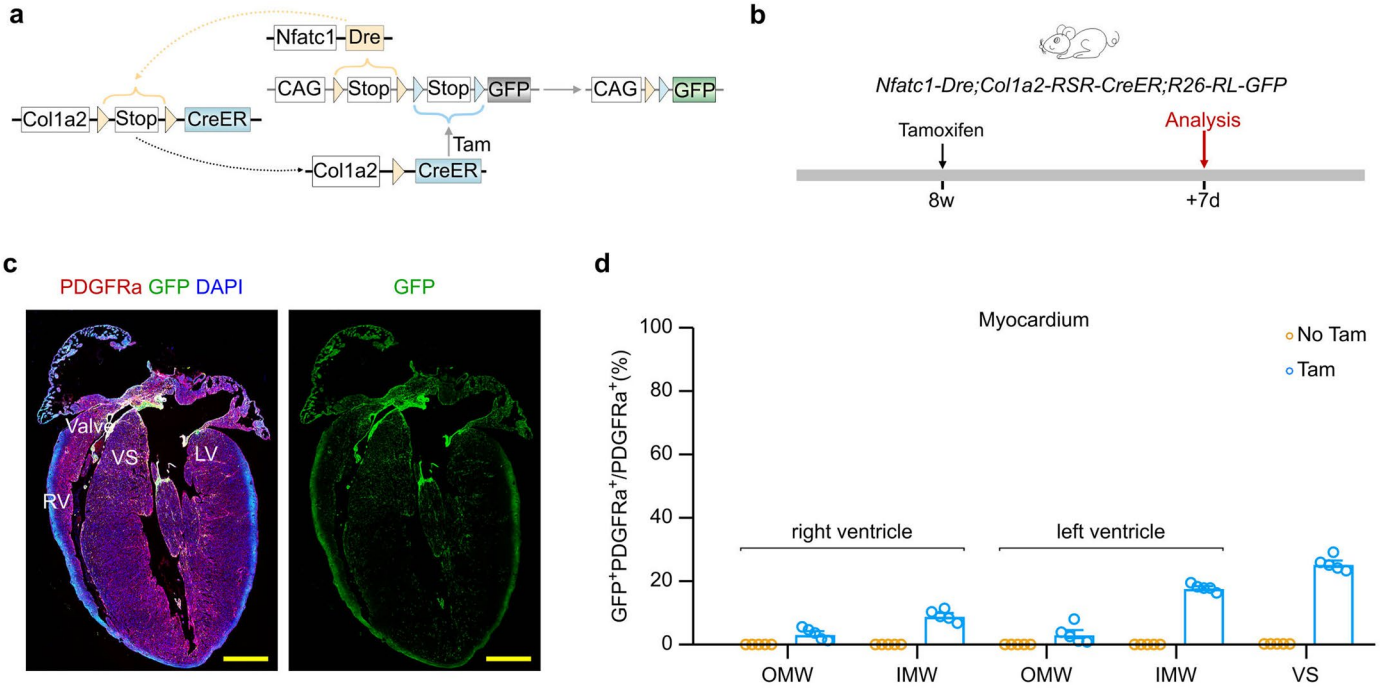

Extended Data Fig. 9 | Characterization of *Col1a2-RSR-CreER* mouse. a, Schematic figure showing rox-flanked Stop cassette removal from *Col1a2-RSR-CreER* and *R26-RL-GFP* by *Nfatc1-Dre*, and loxP-flanked Stop cassette removal from *R26-RL-GFP* by *Col1a2-RSR-CreER* after injecting tamoxifen (Tam). **b**, Schematic figure showing the experimental design. **c**, Immunostaining of PDGFRa and GFP on whole heart sections. **d**, Quantification of the percentage of GFP^+ cells expressing PDGFRa in different regions of hearts. Data are mean ± s.e.m.; $n = 5$ mice. **e-h**, Magnifications of different regions on heart sections. VS, ventricular septum; RV, right ventricle; LV, left ventricle; OMW: outer myocardium wall; IMW, inner myocardium wall. Scale bar: yellow, 1 mm; white, 100 μm. Each image is representative of five individual mouse samples.

https://doi.org/10.1038/s41588-023-01337-7

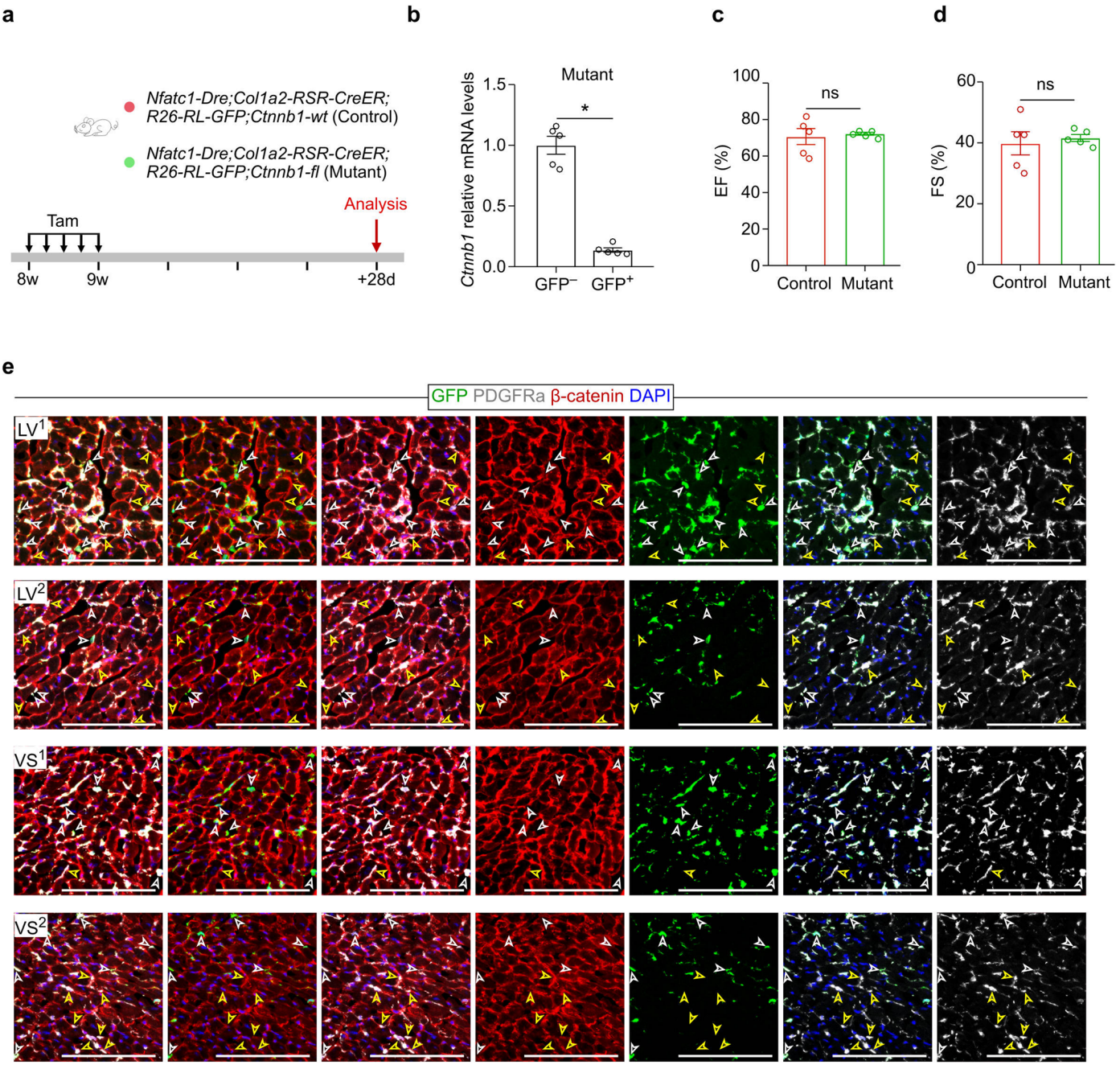

Extended Data Fig. 10 | Knockout of *Ctnnb1* in EndoFb by dual recombinases. **a**, Schematic figure showing the experimental design. **b**, qRT-PCR of *Ctnnb1* expression in GFP⁻ and GFP⁺ fibroblasts sorted from the mutant mice. Data are mean ± s.e.m.; $n = 5$ mice; $^*P < 0.0001$. **c, d**, Quantification of ejection fraction (EF) and fractional shortening (FS) of the control and mutant mice. Data are mean ± s.e.m.; $n = 5$ mice; ns, no significance. **e**, Immunostaining for PDGFRa, β-catenin, and GFP on different parts of hearts collected from the mutant mice. Yellow arrowheads, GFP⁻ β-catenin⁺ PDGFRa⁺ cells; white arrowheads, GFP⁺ β-catenin⁻ PDGFRa⁺ cells. Scale bars, 100 μm. Each image is representative of five individual mouse samples. Unpaired Student's *t*-test was performed in **b-d**.

nature portfolio

Corresponding author(s): Bin Zhou

Last updated by author(s): Jan 23, 2023

Reporting Summary

Nature Portfolio wishes to improve the reproducibility of the work that we publish. This form provides structure for consistency and transparency in reporting. For further information on Nature Portfolio policies, see our Editorial Policies and the Editorial Policy Checklist.

Please do not complete any field with "not applicable" or n/a. Refer to the help text for what text to use if an item is not relevant to your study.
For final submission: please carefully check your responses for accuracy; you will not be able to make changes later.

Statistics

For all statistical analyses, confirm that the following items are present in the figure legend, table legend, main text, or Methods section.

n/a	Confirmed	
	☒	The exact sample size (*n*) for each experimental group/condition, given as a discrete number and unit of measurement A statement on whether measurements were taken from distinct samples or whether the same sample was measured repeatedly
	☒	The statistical test(s) used AND whether they are one- or two-sided *Only common tests should be described solely by name; describe more complex techniques in the Methods section.*
	☒	A description of all covariates tested
☒		A description of any assumptions or corrections, such as tests of normality and adjustment for multiple comparisons
	☒	A full description of the statistical parameters including central tendency (e.g. means) or other basic estimates (e.g. regression coefficient) AND variation (e.g. standard deviation) or associated estimates of uncertainty (e.g. confidence intervals)
	☒	For null hypothesis testing, the test statistic (e.g. *F*, *t*, *r*) with confidence intervals, effect sizes, degrees of freedom and *P* value noted *Give P values as exact values whenever suitable.*
	☒	For Bayesian analysis, information on the choice of priors and Markov chain Monte Carlo settings For hierarchical and complex designs, identification of the appropriate level for tests and full reporting of outcomes
☒		Estimates of effect sizes (e.g. Cohen's *d*, Pearson's *r*), indicating how they were calculated
☒		*Our web collection on statistics for biologists contains articles on many of the points above.*

Software and code

Policy information about availability of computer code

Data collection	Zeiss stereoscope (Axio Zoom. V16) were used for whole-mount bright-field and fluorescence image collection. Olympus fluorescence microscope (B53) were used for collecting the Sirius Red staining pictures and H & E staining pictures. Nikon A1 confocal were used for immunofluorescence data collection. Sony MA900 Flow Cytometer and the Beckman Moflo Astrios EQ Flow Cytometer were used for sorting single cell. Beckman CytoFlex3 was used to do FACS analysis. The Thermo Fisher Scientific, QuantStudio 6 was used to get the qPCR data. The echocardiography imaging system (Vevo 3100, Visual Sonics) was used to get cardiac function (eg. EF, FS) data.
Data analysis	Image J (Fiji)(2.3.0/1.53q) and Photoline (21.00) were used for immunofluorescence and bright-filed images analysis. FlowJo 10.4 (Java Version: 1.8.0_144-b01) were used for FACS data analysis. GraphPad Prism 8.0.0 was used for data analysis. Vevo3100 Imaging Software V3.2.7 was used for calculating cardiac functional parameters. Trim Galore (v0.6.7), STAR (v2.7.0e), samtools (v1.13), ggplot2 R package (v3.3.6), pheatmap R package (v1.0.12), DEseq2 R package (v1.34.0), clusterProfiler R package (v4.2.2) were used for bulk RNA-seq analysis. Analysis of differentially expressed genes was performed using DESeq2. ClusterProfiler investigated the enrichment of gene ontology and annotation.

For manuscripts utilizing custom algorithms or software that are central to the research but not yet described in published literature, software must be made available to editors and reviewers. We strongly encourage code deposition in a community repository (e.g. GitHub). See the Nature Portfolio guidelines for submitting code & software for further information.

Data

Policy information about availability of data

All manuscripts must include a data availability statement. This statement should provide the following information, where applicable:

- Accession codes, unique identifiers, or web links for publicly available datasets
- A description of any restrictions on data availability
- For clinical datasets or third party data, please ensure that the statement adheres to our policy

All data generated by this study are included in this article and it's supplementary materials. They are available upon request. Source data are provided with this paper. The accession number for the raw sequencing data reported in this paper is NCBI Sequence Read Archive: BioProject ID PRJNA813322.

Field-specific reporting

Please select the one below that is the best fit for your research. If you are not sure, read the appropriate sections before making your selection.

☒ Life sciences ☐ Behavioural & social sciences ☐ Ecological, evolutionary & environmental sciences

For a reference copy of the document with all sections, see nature.com/documents/nr-reporting-summary-flat.pdf

Life sciences study design

All studies must disclose on these points even when the disclosure is negative.

Sample size	All experiments were repeated at least three times with similar results. Each sample size were described in detail in each figure legend. No statistical methods were used to predetermine the sample size. A minimum number of animals were used according to standard scientific conventions.
Data exclusions	No data were excluded.
Replication	For each experiment, at least 3 repeats were done to confirm the reproducibility of the findings and all the replication attempts were successful. n means biological replicates (number of mice) and is indicated in the manuscript.
Randomization	For all animal experiments, experimental and control animals were randomly allocated from the appropriated genotype. Samples were allocated randomly to different experimental groups.
Blinding	For image acquisition as well as analysis such as quantification by IF and IHC images, the investigators were blinded. For Echo experiments, the investigators were blinded to record the image data and analysis the data by the Vevo3100 Imaging Software V3.2.7. Investigators were not blinded to mouse treatment and sacrifice because mouse treatment and sacrifice were performed by same people. Investigators were not blinded for bulk-seq analyses studies as there were not separate groups or the sample were annotated. For qPCR, the investigators were not blinding when loading the sample to display the results in a logical way.

Reporting for specific materials, systems and methods

We require information from authors about some types of materials, experimental systems and methods used in many studies. Here, indicate whether each material, system or method listed is relevant to your study. If you are not sure if a list item applies to your research, read the appropriate section before selecting a response.

Materials & experimental systems

n/a	Involved in the study
☐	☒ Antibodies
☒	☐ Eukaryotic cell lines
☒	☐ Palaeontology and archaeology
☐	☒ Animals and other organisms
☒	☐ Human research participants
☒	☐ Clinical data
☒	☐ Dual use research of concern

Methods

n/a	Involved in the study
☒	☐ ChIP-seq
☐	☒ Flow cytometry
☒	☐ MRI-based neuroimaging

Antibodies

Antibodies used

PDGFRa (R&D, Cat# AF1062, 1:100)
GFP (Abcam, Cat# ab6662, 1:500)
Vimentin (Cell signaling technology, Cat# 5741s, 1:100)
aSMA (Abcam, Cat# ab5694,1:100)

tdTomato (Rockland,Cat# 600-401-379,1:1,000)
WT1 (Santa Cruz, Cat# sc-393498, 1:100)
ZsGreen (Clontech, Cat# 632474, 1:1000) TNNI3
(Abcam, Cat# ab56357, 1:200)
CD31 (BD Pharmingen, Cat# 553370, 1:500)
VE-Cad (R & D, Cat# AF1002, 1:100)
human HB-EGF(DTR)(R & D, Cat# AF-259-NA, 1:100)
WGA (Invitrogen, Cat# W32466, 1:1,000)
β-catenin (BD Pharmingenp, Cat# 610153, 1:200)
Alexa donkey anti-rabbit 555 (Invitrogen, Cat# A31572, 1:1,000)
Alexa donkey anti-rabbit 488 (Invitrogen, Cat# A21206, 1:1,000)
Alexa donkey anti-goat 488 (Invitrogen, Cat# A11055, 1:1,000)
Alexa donkey anti-goat 555 (Invitrogen, Cat# A32816, 1:1,000)
Alexa donkey anti-goat 647 (Invitrogen, Cat# A21447; 1:1000)
Alexa donkey anti-mouse 555 (Invitrogen, Cat# A31570, 1:1,000)
HRP donkey anti-rat (JIR, Cat# 712-035-153, 1:100)
Immpress horse anti-goat (Vector lab, Cat# MP-7405, 1:1)
Cyanine 3 Amplification Reagent (PerkinElmer, Cat# NEL744001KT, 1:1,000)
Cyanine 5 Amplification Reagent (PerkinElmer, Cat# NEL745001KT, 1:1,000)
Fluorescein Amplification Reagent (PerkinElmer, Cat# NEL741001KT, 1:1,000)
anti-Ter-119 PE-Cy7 (eBioscience, Cat# 25-5921, 1:200)
anti-CD45 PE-Cy7 (eBioscience, Cat# 25-0451, 1:400)
anti-CD140a APC (BD pharmingen, Cat# 562777, 1:40)
anti-CD31 APC (eBioscience, Cat# 17-0311-80, 1:40)

Validation

Validation statements are available from manufactuer's websites:
PDGFRa (R&D, Cat# AF1062, 1:100); https://www.novusbio.com/products/pdgfr-alpha-antibody_af1062
GFP (Abcam, Cat# ab6662, 1:500); https://www.abcam.com/fitc-gfp-antibody-ab6662.html
Vimentin (Cell signaling technology, Cat# 5741s, 1:100); https://www.cellsignal.com/products/primary-antibodies/vimentin-d21h3-xp-rabbit-mab/5741
aSMA (Abcam, Cat# ab5694, 1:100); https://www.abcam.com/alpha-smooth-muscle-actin-antibody-ab5694.html
tdTomato (Rockland, Cat# 600-401-379, 1:1000); https://www.rockland.com/categories/primary-antibodies/rfp-antibody-pre-adsorbed-600-401-379/
WT1 (Santa Cruz, Cat# sc-393498, 1:100); https://www.scbt.com/p/wt1-antibody-c-19/
ZsGreen (Clontech, Cat# 632474, 1:1000); https://www.takarabio.com/products/antibodies-and-elisa/fluorescent-protein-antibodies/green-fluorescent-protein-antibodies?catalog=632474
TNNI3 (Abcam, Cat# ab56357, 1:200); https://www.abcam.com/cardiac-Troponin-I-antibody-ab56357.html
CD31 (BD Pharmingen, Cat# 553370, 1:500); http://www.bdbiosciences.com/us/applications/research/stem-cell-research/cancer-research/mouse/purified-rat-anti-mouse-cd31-mec-133/p/553370
VE-Cad (R & D, Cat# AF1002, 1:100); http://www.rndsystems.com/Products/af1002/RelatedInformation
human HB-EGF(DTR)(R & D, Cat# AF-259-NA, 1:100); https://www.rndsystems.com/cn/products/human-hb-egf-antibody_af-259-na
WGA (Invitrogen, Cat# W32466, 1:1,000); https://www.thermofisher.cn/order/catalog/product/W32466
β-catenin (BD Pharmingenp, Cat# 610153, 1:200); https://www.citeab.com/antibodies/2413593-610153-bd-transduction-laboratories-purified-mouse
Alexa donkey anti-rabbit 555 (Invitrogen, Cat# A31572, 1:1,000); https://www.thermofisher.cn/cn/zh/antibody/product/Donkey-anti-Rabbit-IgG-H-L-Highly-Cross-Adsorbed-Secondary-Antibody-Polyclonal/A-31572
Alexa donkey anti-rabbit 488 (Invitrogen, Cat# A21206, 1:1,000); https://www.thermofisher.cn/cn/zh/antibody/product/Donkey-anti-Rabbit-IgG-H-L-Highly-Cross-Adsorbed-Secondary-Antibody-Polyclonal/A-21206
Alexa donkey anti-goat 488 (Invitrogen, Cat# A11055, 1:1,000); https://www.thermofisher.cn/cn/zh/antibody/product/Donkey-anti-Goat-IgG-H-L-Cross-Adsorbed-Secondary-Antibody-Polyclonal/A-11055
Alexa donkey anti-goat 555 (Invitrogen, Cat# A32816, 1:1,000);https://www.thermofisher.cn/cn/zh/antibody/product/Donkey-anti-Goat-IgG-H-L-Highly-Cross-Adsorbed-Secondary-Antibody-Polyclonal/A32816
Alexa donkey anti-goat 647 (Invitrogen, Cat# A21447, 1:1000); https://www.thermofisher.cn/cn/zh/antibody/product/Donkey-anti-Goat-IgG-H-L-Cross-Adsorbed-Secondary-Antibody-Polyclonal/A-21447
Alexa donkey anti-mouse 555 (Invitrogen, Cat# A31570, 1:1,000);https://www.thermofisher.cn/cn/zh/antibody/product/Donkey-anti-Mouse-IgG-H-L-Highly-Cross-Adsorbed-Secondary-Antibody-Polyclonal/A-31570
HRP donkey anti-rat (JIR, Cat# 712-035-153, 1:100); https://www.jacksonimmuno.com/catalog/products/712-035-153
Cyanine 3 Amplification Reagent (PerkinElmer, Cat# NEL744001KT, 1:1,000); https://my.akoyabio.com/ccrz ProductDetails?viewState=DetailView&sku=NEL744001KT
Cyanine 5 Amplification Reagent (PerkinElmer, Cat# NEL745001KT, 1:1,000); https://my.akoyabio.com/ccrz ProductDetails?sku=NEL745001KT&cclcl=en_US
Fluorescein Amplification Reagent (PerkinElmer, Cat# NEL741001KT, 1:1,000); https://my.akoyabio.com/ccrz ProductDetails?sku=NEL741001KT&cclcl=en_US
Immpress horse anti-goat (Vector lab, Cat# MP-7405, 1:1); https://www.novusbio.com/products/igg-immpress-tm-antibody_mp-7405-nb
anti-Ter-119 PE-Cy7 (eBioscience, Cat# 25-5921, 1:200); https://www.thermofisher.cn/cn/zh/antibody/product/TER-119-Antibody-clone-TER-119-Monoclonal/25-5921-82
anti-CD45 PE-Cy7 (eBioscience, Cat# 25-0451, 1:400); https://www.thermofisher.cn/cn/zh/antibody/product/CD45-Antibody-clone-30-F11-Monoclonal/25-0451-82
anti-CD140a APC (BD pharmingen, Cat# 562777, 1:100); https://www.bdbiosciences.com/en-us/products/reagents/flow-cytometry-reagents/research-reagents/single-color-antibodies-ruo/apc-rat-anti-mouse-cd140a.562777
anti-CD31 APC (eBioscience, Cat# 17-0311-80, 1:40); https://www.thermofisher.com/antibody/product/CD31-PECAM-1-Antibody-clone-390-Monoclonal/17-0311-80

Animals and other organisms

Policy information about studies involving animals; ARRIVE guidelines recommended for reporting animal research

Laboratory animals	Mice of both male and female at the age of 8-20 weeks were used for experiments with similar aged mice for both control and experimental groups. All mice were maintained on a 129, C57BL6 and ICR mixed background. All mice were housed at the laboratory Animal center of the Center for Excellence in Molecular Cell Science in a Specific Pathogen Free (SPF) facility with individually ventilated cages. The room has controlled temperature (20-25°C), humidity (30%-70%) and light (12 hour light-dark cycle). Mice were provided ad libitum access to a regular rodent chow diet.
Wild animals	No wild animals were included in this study.
Field-collected samples	No field-collected samples were included in this study.
Ethics oversight	All mice were used in accordance with the guidelines of the Institutional Animal Care and Use Committee (IACUC) of Shanghai Institute of Biochemistry and Cell Biology, Chinese Academy of Sciences.

Note that full information on the approval of the study protocol must also be provided in the manuscript.

Flow Cytometry

Plots

Confirm that:

☐ The axis labels state the marker and fluorochrome used (e.g. CD4-FITC).

☐ The axis scales are clearly visible. Include numbers along axes only for bottom left plot of group (a 'group' is an analysis of identical markers).

☐ All plots are contour plots with outliers or pseudocolor plots.

☒ A numerical value for number of cells or percentage (with statistics) is provided.

☒

Methodology

Sample preparation	Cardiac fibroblasts were isolated from hearts as described previously(Skelly et al., 2018; Zhang et al., 2021). The reagents used in cell isolation include PBS (Gibco, C10010500BT), FBS (Gibco, A3161001C), HBSS (Gibco, 14025092), Collagenase IV (Gibco, 17104019), Dispase (BD Biocoat, 354235), DNase I (Worthington Biochemical Corporation, LS002139), and DMEM (Gibco, 11965092). Before sacrificing the mice with CO2, buffers including washing buffer (PBS with 0.8 mmol/L CaCl2), staining buffer (2%FBS in HBSS), and digestion solution (2 mg/mL Collagenase IV and 1.2 U/mL Dispase in washing buffer) were prepared and put in ice already. Once mice died, the chest was opened and the heart was perfused with 20 ml washing buffer through the right ventricle to wash out the blood cells in the hearts. The heart was isolated from the body and put in the dish including washing buffer, then removed the atria and valve, and the ventricle was placed in a 1.5 ml centrifuge tube with digestion solution, then cut the tissues into small pieces. After mincing, transfer the tissues in a 15 ml centrifuge tube with 3ml digestion solution, and put the tube at 37 ℃ with a certain oscillation frequency for 25~40min. Tissue suspensions were blown with straws every 8 minutes. Filter the cell suspension with a 70 μm filter into a 50 ml centrifuge tube, then rinse the filter with 3 ml washing buffer to stop the digestion reaction, the put the tube into a 4 ℃ centrifuge at 400g for 5min to get the cell precipitation. The cell precipitation was resuspended with 4 ml staining buffer and centrifuged at 4 ℃ with 400g for 5min. Afterward, the cell precipitation was resuspended with 300 μl staining buffer, then we got the isolated cells.
Instrument	Sony MA900 Flow Cytometer; Beckman CytoFlex3; Beckman Moflo Astrios EQ
Software	FlowJo 10.4 (Java Version: 1.8.0_144-b01)
Cell population abundance	About 1X10^7 non-cardiomyocyte cells were analysis. cardiac fibroblasts comprise about 15% of the single cell suspension.
Gating strategy	First, remove small debris in FSC-A verse SSC-A gating. And then doublets were excluded in SSC-A verse SSC-H gating. Dead cells were excluded on DAPI staining. Blood cells were exclued on CD45 and Ter-119 staining. Then fibroblast population was collected in gates determined on CD140a antibody staining, and the endothelium cells population was collected in gates determined on CD31 antibody staining. The counting beads were gated as the guideline suggested. The EndoFb and other fibroblasts were distinguished by GFP.

☒ Tick this box to confirm that a figure exemplifying the gating strategy is provided in the Supplementary Information.